Fault growth mechanisms and scaling properties in foreland basin system: The case study of Monte Alpi, Southern Apennines, Italy

Vincenzo La Bruna, Fabrizio Agosta, Juliette Lamarche, Sophie Viseur, Giacomo Prosser

Fault growth mechanisms and scaling properties in foreland basin system: The case study of Monte Alpi, Southern Apennines, Italy

Vincenzo La Bruna[1-2], Fabrizio Agosta[2], Juliette Lamarche[1], Sophie Viseur[1], Giacomo Prosser[2]

[1]CEREGE-UMR 34, Aix-Marseille University, Marseille, France

[2]Department of Sciences, University of Basilicata, Italy

Corresponding author: Vincenzo La Bruna (vincenzolabruna@gmail.com)

Key words: syn-sedimentary faults, orthogonal fault system; fault dimensional properties, Apulian Platform, 3D geological reconstruction.

Abstract

The present work focuses on the comprehension of the growth mechanisms and dimensional properties of the pre-Pliocene Monte Alpi fault network by mean of integrated field and laboratory analyses. After this multidisciplinary approach, detailed throw profiles are computed for each fault belonging to the Monte Alpi network. Subsequently, the dimensional properties of the individual faults are calculated. Data obtained from this work are discussed in terms of fault growth mechanisms and timing of deformation, and reported in a conceptual tectonic evolution model of the Messinian foreland basin system. Data suggest that originally isolated fault segments developed during the earliest stages of foreland basin formation by re-activation of a pre-existing, Early Cretaceous fault set, and formation of an orthogonal one. These two fault sets formed a scale-independent network. Differently, the same fault sets were also active during its subsequent development forming a scale-dependent fault network

characterized by T- and Y-shaped fault intersections. This deformation controlled the half-graben depocenters evolution filled by up to ca. 600 meters of terrigenous deposits during the Late Messinian time.

1. Introduction

Numerous studies have shed light on the evolution of the foreland basin systems flanking orogenic belts, but some gaps remain in particular related to the understanding of the fault growth mechanism and fault dimensional properties related to the structural networks that control the foreland basin system evolution. This knowledge is important to decipher the modalities of the extensional deformation associated to foreland flexure, which is commonly due to migration of Fold-and-Thrust belts (FTB), and unveil the possible role exerted by pre-existing, inherited faults on development of foreland basin systems (Gawthorpe and Leedert, 2000). As documented in literature, longitudinal extensional faults parallel to the main thrust front of the FTB are frequently observed across the whole foreland basin system (Harding and Tuminas, 1989; Lorenzo et al., 1998; Ranero et al., 2003). Moreover, subordinated transverse extensional faults, which are perpendicular to the main thrust front can develop because of the stress release in the fault hanging wall of longitudinal faults (Destro, 1995; Medwedeff and Krantz 2002; Tavani et al., 2015), or be present as transfer faults within linked extensional systems (Tavarnelli et al., 1999).

Subsequently, during the migration of the orogenic chain this inner portion of the foreland basin system and its orthogonal fault network could experience orogenic compression and incorporated in FTBs.

In this paper, we present the results of a study performed in the Monte Alpi area which represent a key tectonic window of the southern Apennines FTB of Italy (Alberti et al., 2001; Patacca and Scandone, 2007). There, Mesozoic carbonates pertaining to the Inner Apulian

Platform (Sartoni and Crescenti, 1962) and overlapping Lower Messinian carbonates and Upper Messinian siliciclastic rocks (Sgrosso, 1988; Taddei and Siano, 1992) crop out in the axial portion of the belt (Cello and Mazzoli, 1998).

This peculiar site represents a unique opportunity to study and unveil the structural control exerted by an orthogonal fault network which controlled the evolution of the Messinian foreland basin system (Patacca et al.,1992), subsequently involved in several tectonic phases (Van Dijk et al., 2000; Mazzoli et al., 2006; La Bruna et al., 2017).

The results of this work may provide useful insights in order to better assess the timing of formation of the two aforementioned high-angle fault sets, which pre-date Early-Middle Pliocene contractional deformation associated to the FTB migration (Patacca and Scandone, 2007). In particular, data obtained after a detailed field structural and stratigraphic analyses are employed, together with available subsurface data, to perform 3D geological reconstruction of a ca. 320 km^2 wide area. As a result, both attitude and cumulative throw profiles are computed for the individual, outcropping, high-angle faults crosscutting the Monte Alpi Unit. By also considering the displacement of specific chronostratigraphic surfaces, the dimensional properties of the evolving pre-Pliocene fault network are discussed in terms of either scale-independent (Schultz et al., 2008) or scale-dependent geometries (Kim and Sanderson, 2005). In fact, as described in literature, when initially isolated fault segments interact and, possibly, link together during ongoing deformation, they modify their dimensional properties (Walsh and Watterson, 1988; Peacock and Sanderson, 1991; Cartwright et al., 1995; Dawers and Anders, 1995; Mansfield and Cartwright, 1996; Crider and Pollard, 1998; Cowie and Roberts, 2001; Walsh et al., 2003). Considering the following relationship between the maximum fault cumulative displacement (D) and its maximum linear dimension (L, length)

$$D=cL^n \quad \text{(eq. 1)}$$

where the *c* value is related to the rock mechanical properties, it is possible to assess the geometrical properties of the fault network by considering the *n* value (Watterson, 1986; Walsh and Watterson, 1988; Cowie and Scholz, 1992a,b; Scholz et al., 1993; Schlische et al., 1996; Kim and Sanderson, 2005; Schultz et al., 2008). Values of $n=1$ indicate a linear scaling law (i.e. self-similarity), which implies that faults grew under conditions of constant driving stress at different scales, whereas values of $n>1$ suggest a scale-dependent geometry. Regarding the study area of Monte Alpi, the contribution provided by the different angles among intersecting faults forming a scale dependent geometry is investigated by considering both T- and Y-shaped intersections (Maerten et al., 1999). Finally, evolution of the pre-Pliocene fault network is summarized in a conceptual model of Messinian foreland basin system evolution by taking the computed time-dependent activity of individual fault sets into account (sensu Gawthorpe and Leedert, 2000).

2. Geological setting

2.1 Southern Apennines

The Apennines are an arc-shaped FTB that formed in response to the Oligocene-to-Pliocene continental collision between Eurasian and African lithospheric plates (Royden et al., 1987; Locardi, 1988). Such a process caused the formation of east-propagating thrust sheets, which involved Meso-Cenozoic terranes originally pertaining to the Neo-Tethys Ocean, and of its south-eastern continental margin, and/or to the subduction-related accretionary wedge (Patacca et al., 1990; Doglioni, 1991). Commonly, the Apennines are sub-divided along-strike into three sectors named as northern, central, and southern, respectively, bounded by lithospheric discontinuities trending at high-angles with respect to the belt axis (Locardi, 1988; Ghisetti and Vezzani, 1997; Vai and Martini, 2001; Cavazza et al., 2004; Patacca and Scandone, 2007). Most of the paleogeographic models proposed for the Mesozoic Neo-Tethys

ocean invoked two main carbonate platforms commonly identified as Apenninic, to the west, and Apulian, to the east, separated from each other by communicating basins (D'Argenio et al., 1972; Ippolito et al., 1975; Mostardini and Merlini, 1986; Tavarnelli and Prosser, 2003; Schettino and Turco, 2011).

The current structural setting of the southern Apennines FTB includes the following tectono-stratigraphic units, from the top to the bottom, which respectively correspond to specific paleogeographic domains arranged from west to east, respectively (Patacca and Scandone, 2007): i) siltstones and claystones originally pertaining to the Liguride/Sicilide oceanic Basin; ii) carbonates derived from the Apennine Platform; iii) mixed terrigenous-carbonate rocks derived from the Lagonegro basin, divided into two different tectonic Units, Lagonegro I and II; and iv) carbonates of the Apulian Platform (Figure 1). Miocene-to-Pliocene terrigenous infill of foredeep, thrust-top, and piggyback basins were involved in contractional deformation, and currently crop out in the axial and outer portions of the belt (Ghisetti and Vezzani, 1981; Dewey et al., 1989; Boccaletti et al., 1990; Carbone et al., 1990; Van Dijk and Okkes, 1990, 1991; Monaco and Tanzi, 1992; Catalano et al., 1993; Monaco and Tortorici, 1995; Monaco et al., 1998; Pescatore et al., 1999; Menardi Noguera and Rea, 2000; Patacca and Scandone, 2007). The Inner Apulian Platform was involved in Late Pliocene-Early Pleistocene thick-skinned tectonics (Mostardini and Merlini, 1986; Cello and Mazzoli, 1998; Butler et al., 2004; Shiner et al., 2004), whereas the Outer Apulian Platform is now days either exposed or buried underneath a Plio-Pleistocene sedimentary cover in the orogenic foreland of the Southern Apennines (Pieri et al., 1997; Borgomano, 2000; Spalluto, 2012; Panza et al., 2016; Petrullo et al., 2017). (insert Figure 1).

124 *2.2 Monte Alpi Unit*

125 The study area is located in the axial portion of the southern Apennines FTB (Figure 1). Over
126 the years, according to the presumed age of the sedimentary cover, many authors proposed
127 two conflicting hypotheses on the origin of the Monte Alpi carbonates. Assigning a Lower
128 Miocene age to its sedimentary cover, the Mesozoic carbonates were interpreted as part of the
129 Apennine Platform (Ogniben, 1969; Mostardini and Merlini, 1986; Muller et al., 1988).
130 Differently, by assigning a Messinian age, other authors included them in the Inner Apulian
131 Platform (Carbone et al., 1988; Sgrosso, 1988; Van Dijk et al., 2000; Alberti et al., 2001;
132 Mazzoli et al., 2006, 2014). Structurally, the two most recent studies interpreted Monte Alpi
133 as comprised of Apulian carbonates either forming a push-up structure (Van Dijk et al., 2000)
134 or as the product of complex thin- and thick-skinned tectonics (Shiner et al., 2004; Mazzoli et
135 al., 2006, 2014).
136 According to their inferred age of activity, La Bruna et al. (2017) recognized six different
137 structural networks and documented two main sets of high-angle faults pre-dating Early-
138 Middle Pliocene emplacement of the allochthon over the Mesozoic carbonates and their
139 Upper Miocene cover (Cello and Mazzoli 1998; Buttler et al., 2004). The two high-angle fault
140 sets formed an almost orthogonal fault system, which developed during either Cretaceous
141 strike-slip and dip-slip tectonics (Pieri and Laviano, 1989; Festa et al., 2003; Mazzoli et al.,
142 2006; Bertok et al., 2012; Tavani et al., 2013; Korneva et al., 2014; Panza et al., 2015, 2016;
143 Laurita et al., 2016; Vitale et al., 2017), or Upper Miocene foreland bulging (Doglioni et al.,
144 1995) and/or along-foredeep stretching (Tavani et al., 2015a).
145 The Monte Alpi Unit is made up of ca. 2,000 m-thick, Jurassic-to-Lower Cretaceous
146 limestones and dolostones, and Messinian carbonates-terrigenous rocks (Figure 2). The
147 Jurassic carbonates are Middle-to-Upper Jurassic in age, whereas the Lower Cretaceous ones
148 are ascribed to the Neocomian (De Lorenzo, 1895; Selli, 1957; Sartoni and Crescenti, 1962;

149 Grandjacquet, 1963; Roda, 1965; Ogniben, 1969). The Messinian sedimentary succession is
150 stacked into two main intervals (Sgrosso et al., 1988; Ortolani and Torre, 1971; Taddei and
151 Siano, 1992; Van Dijk et al., 2000). The Lower Messinian deposits, which form a
152 paraconformity with the Lower Cretaceous carbonates, consist of up to 35 m-thick skeletal
153 grainstones and minor packstones, floatstones, rudstones and bindstones. Differently, the
154 Upper Messinian deposits, which form a 3° to 5° angular unconformity with both Lower
155 Messinian and Lower Cretaceous carbonates, include polygenic conglomerates, litharenitic
156 sandstones, and siltstones characterized by remarkable thickness and compositional
157 variations. (insert Figure 2).
158
159 **3. Data and Methods**
160 The proposed integrated approach includes a variety of methods such as geological mapping,
161 field structural and stratigraphic analyses, well log correlation, seismic profile interpretation,
162 and 3D surfaces reconstruction.
163 *3.1 Field analysis*
164 The large-scale geological map was compiled at a 1:25,000 scale (Figure 2) by taking into
165 account available published data (Foglio IGM 211, S. Arcangelo; Bonardi et al., 2009;
166 Cavalcante et al., 2009; Lentini, 1991), and the detailed geological map originally compiled at
167 a 1:10,000 scale by La Bruna et al. (2017). Field structural analyses focused on the fault zones
168 exposed in the Monte Alpi area. Eight stratigraphic logs were measured in key sites, which
169 expose significant portions of the Lower and Upper Messinian deposits.
170
171 *3.2 Seismic profile interpretation*
172 Interpretation of the four stacked seismic reflection profiles (courtesy of Eni) was aimed at
173 deciphering the geometry of the buried Apulian carbonates (Figure 3). Due to the general

poor quality of the seismic profiles, such an interpretation was compared with published well log data, seismic reflection profile and isobaths maps (Mazzoli et al., 2006, 2014; Nicolai and Gambini, 2007). The original jpeg images were first converted into seg-y files, by using the image2segy 2.2.6 Matlab script developed by the Instituto de Ciències del Mar (Barcelona, Spain), and then imported into the Move™ software for subsequent digitalization of the main stratigraphic horizons and fault surfaces. Afterwards, the time-to-depth conversion was computed by assigning a specific velocity value to the individual tectono-stratigraphic units (Dix, 1955; Improta et al., 2000). (insert Figure 3).

3.3 3D geological reconstruction

This work involved several steps of activities aimed at reconstructing both stratigraphic and tectonic surfaces pertaining to the Monte Alpi Unit. First, the Digital Elevation Model (DEM), the large-scale geological map, and all the available subsurface data in jpeg format were imported into Gocad®, and then georeferenced for calibration and consistency checking. The imported DEM was characterized by a 20x20 m resolution. A triangulated mesh was built from the DEM data points using both the Delaunay triangulation and interpolation in order to obtain a continuous and optimized representation of the topography (Mallet et al., 2002). Then, the georeferenced geological map was draped onto the topographic surface to obtain a textured topographic surface.

In order to constrain the buried portions of the Apulian carbonates, we performed time-to-depth conversion of four seismic profiles by using the GeolToolbox plugin (www.ring-team.org/consortium). Furthermore, six geological cross-sections obtained from the published geological map of Monte Alpi (La Bruna et al., 2017) and existing bibliography related to geometry of the buried Top Apula surface underneath the southern Apennines FTB (Niccolai and Gambini, 2007) were taken into account. The eight stratigraphic logs performed in

199 correspondence of the outcropping mixed carbonate-terrigenous Messinian cover were also
200 imported in GOCAD. The 3D geological model of Monte Alpi was finally obtained by
201 constructing the individual fault and stratigraphic surfaces by using the Discrete Smooth
202 Interpolation tool (Mallet, 1989; Mallet et al., 2002), which allowed to constrain on fault-fault
203 and fault-stratigraphic surfaces in the light of the aforementioned data. Both resolution and
204 convergence criteria were defined according to the protocol recommended by Caumon et al.,
205 (2009).
206
207 *3.4 Fault analysis*
208 Fault throw computation for individual faults was carried out by considering the cutoff lines
209 along the fault hanging walls (Figure 4). This data was obtained by following the
210 aforementioned procedure, in which the individual stratigraphic surfaces were cut by the
211 high-angle fault surfaces. Subsequently, as a first step, the total amount of throw distribution
212 (cumulative throw) was computed for each fault surface. This value corresponded to the
213 current vertical offset of the bottom Early Cretaceous surface. Then, the pre-Messinian throw
214 distribution was calculated by subtracting the amount of Early Messinian vertical
215 displacement from the cumulative throw. Similarly, the Early Messinian throw data were
216 obtained by subtracting the amount of Late Messinian vertical displacement from the pre-
217 Messinian throw data. (insert Figure 4).
218
219 **4. Results**
220 *4.1 Syn-sedimentary extensional faulting*
221 *I - Mesozoic carbonates*
222 Mid-Upper Jurassic carbonates crop out only along the NW edge of Monte Alpi (Figure 5a),
223 whereas the Lower Cretaceous ones are widespread in the study area (De Lorenzo, 1895;

Selli, 1957; Sartoni and Crescenti, 1962; Grandjacquet, 1963; Roda, 1965; Ogniben, 1969). The former carbonates consist of greyish-to- black limestones and minor dolomites, which are conformably overlain by Lower Cretaceous, peritidal, whitish-to-dark grey limestones showing multiple dissolution evidences such as karst solution grooves and fissures. Both Jurassic and Lower Cretaceous limestone beds are quite tabular, 10's of cm- to m-thick, and commonly consist of grainstones and packstones, and less frequent mudstones, wackestones, bindstones, floatstones and rudstones (Dunham, 1962; Embry and Klovan, 1971). Results of thin section analysis are consistent with abundance of benthic foraminifera, peloids, and fenestral structures within both Jurassic and Lower Cretaceous carbonate rocks (Figures 5b-f). In particular, the Jurassic limestones include cm-sized stromatoporoids (*Cladocoropsis mirabilis,* Figure 5b), whereas the Cretaceous ones contain oolites (Figure 5c) and red algae (*Salpingoporella annulata*, Figures 5d and f). Dolomites are petrographically heterogeneous in texture, crystal size, and crystal shape (Rustichelli, personal communication); late diagenetic fabric-destructive zebra (saddle) dolomites are also documented (Figure 5g). Blocky calcite cement fills the pore space. Calcite veins, rare quartz veins, and dark microstylolites crosscut the Mesozoic carbonates (La Bruna et al., 2017). Along the western cliff of the carbonate massif, within the Lower Cretaceous limestones, a ENE-striking, NNW-dipping, syn-sedimentary normal fault is documented (Figures 5a and h). There, the carbonate succession shows an increase of thickness toward the major slip surface (Figures 5h and i). (insert Figure 5).

II - Lower Messinian carbonates

Up to 35 m-thick, Lower Messinian limestones crop out along both the western cliff of Monte Alpi and the eastern slope of the Santa Croce Peak (cf. Figures 2 and 6a). These limestones consist mainly of grey-to-dark gray skeletal grainstones with minor packstones, floatstones, rudstones and bindstones (Figures 6b-g). Biota is dominated by red algal (*Lithothamniun*)

249 debris with minor benthic foraminifera, echinoid plates and spines, and fragments of serpulids
250 (*Ditrupa*) and bivalves, collectively pointing to an inner-middle ramp depositional setting.
251 The individual limestone beds are tabular, laterally continuous, characterized by a thickness
252 variation comprised between 10's of cm and ca. 4 m, and show thinning upward trends. The
253 topmost portion of the Lower Messinian limestones is made up of thinly-bedded, bituminous,
254 planktonic foraminiferal wackestones including fish remains and intervening marl beds
255 (Figures 6b-f). The Lower Messinian limestones, which include blocky calcite cements, dark
256 stylolites, and multiple sets of calcite veins, were originally deposited in an outer ramp
257 depositional setting, which became progressively deeper with time (Taddei and Siano, 1992;
258 La Bruna et al., 2017). ENE-striking, and both NNW- and SSE-dipping, syn-sedimentary
259 normal faults are exposed along the north-eastern sector of Monte Alpi (Figures 6a and h).
260 These faults produced an accommodation space in their hanging wall in which limestone beds
261 were deposited (Figures 6h and i). The two sets of ENE-striking faults form a conjugate fault
262 system that also crosscut the Lower Cretaceous limestone rocks, causing roll over (higher dip
263 angles towards the faults) of the limestone beds located at the hanging wall of the major,
264 Early Messinian normal fault. (insert Figure 6).

265 *III - Upper Messinian terrigenous deposits*

266 The Upper Messinian siliciclastic beds, which respectively form both onlap and downlap
267 geometries with the high-angle faults and low-angle erosional surfaces crosscutting both
268 Lower Cretaceous and Lower Messinian limestones (Figures 7a and b), are made up of
269 conglomerates, sandstones and siltstones. The heterometric conglomerates include sub-
270 rounded to flattened, polygenic pebbles (Figure 7c), whereas the litharenitic sandstones
271 contain coarse-to-thin rock fragments arranged in either parallel or cross laminated beds
272 (Figure 7d). The former rocks are located at the western and north-eastern edges of Monte
273 Alpi, whereas the sandstones throughout its north-eastern and eastern sectors (La Bruna et al.,

2017). The exposed Upper Messinian succession is up to ca. 300 m-thick. (insert Figure 7). To better decipher its depositional architecture, multiple stratigraphic logs have been measured throughout the study area. Logs #1 to #4 highlight the northward thinning of conglomerates along the southern sector of Monte Alpi, whereas logs #5 to #7 show their westward thinning along its eastern sector (Figure 8). (insert Figure 8).

By considering thickness variations of the Upper Messinian terrigenous deposits, an isopach map of the Upper Messinian deposit is computed, which shows that the two maxima located at the SW and NW edges of Monte Alpi are bound by the F2 and F3 Faults (Figure 9a). A third, less pronounced maximum is also computed at the intersection of the two aforementioned faults. In order to decipher the bedding attitude of both Lower Cretaceous and Lower Messinian limestones at the onset of deposition during Upper Messinian, data are restored accordingly (Figure 9b). Results are consistent with the west- and southwest-dipping limestone beds of the Canale del Grillone area, western sector of Monte Alpi, separated by a structural horst bounded by both F4 and F5 Faults from northeast-dipping beds of the Santa Croce area, eastern sector of Monte Alpi. (insert Figure 9).

4.2 Fault dimensional analysis

The 3D geological model constructed for the whole study area consists of a $2*10^3$ km^3 volume that includes three stratigraphic surfaces pertaining to the Monte Alpi Unit, and forty-three fault surfaces. Both dip azimuth and dip angle data were then computed for the largest, twenty-seven fault surfaces (Figure 10a, Table1). Results are shown with histograms (Figures 10b and 10c). (insert Figure 10 and Table 1). According to their strike direction, the twenty-seven fault surfaces are sorted into the following five sets:

Set 1 - NW-SE faults with throws between 100 and 1,300 m;

Set 2 - NNW-SSE faults with throws between 100 and 1,300 m;

299 Set 3 - ENE-WSW faults with throws between 50 and 800 m;

300 Set 4 - WNW-ESE faults with throws between 170 and 1,100 m;

301 Set 5 - NNE-SSW faults with throws between 50 and 150 m.

302 Results of mesoscale structural analysis performed at specific outcrops have been used to
303 better constrain both attitude and kinematics of individual fault sets, as well as to document
304 their relative abutting and crosscutting relationships (Figure 11). Sets 1 and 2 mainly consist
305 of left-lateral, strike-slip faults, which were then re-activated as normal faults during the latest
306 exhumation stages (La Bruna et al., 2017). Sets 3 and 4 comprise normal faults likely re-
307 activated as reverse faults during Early Pleistocene times (Van Dijk et al., 2000), whereas Set
308 5 only includes normal faults. (insert Figure 11).

309

310 *4.3 Fault throw analysis*

311 Fault throw analysis is carried out by taking the computed cumulative throw (D) and length
312 (L) values into account. Error bars were estimated for the individual fault surfaces (cf. Figure
313 4) on the basis of the resolution obtained. Errors are reported hereafter. *D*: ± 50m (F1, F2, F3
314 and F5 Faults), ± 10m (F4 Fault), ± 5m (F6, F7, F9 and F12 Faults), ± 2m (F8 Fault), ± 1m
315 (F11 Fault), and ± 0,5m (F10 Fault). *L:* ± 50m (F1, F2, F3, F5, F11 and F12 Faults), ± 25m
316 (F4, F6, F7, F8, F9 and F10 Faults).

317 Results of throw-length computations are consistent with different shapes of the fault throw
318 profiles (Fig. 12). In fact, both F10 and F3 faults show symmetric, bell-shaped profiles,
319 whereas F6, F8, and F12 faults are characterized by flat-topped profiles. Moreover, F1, F4,
320 and F11 faults show asymmetric profiles with steep gradients towards one of the fault tips,
321 whereas F2, F5, F7, and F9 faults display asymmetric profiles with steep gradients toward
322 both fault tips. (insert Figure 12).

323 The computed pre-Messinian, Early Messinian, and post-Early Messinian throw profiles are
324 reported in Figure 13, and summarized in the following text (negative values correspond to
325 either reverse displacements or rotated normal faults). (insert Figure 13).
326 F1 Fault (Set 2): the post-Early Messinian throw profile shows an asymmetric shape, with
327 values increasing towards the NNW edge; along the central portion of the fault, the profile is
328 flat-topped. The Early Messinian throw profile does not record any displacement, whereas the
329 pre-Messinian throw profile shows two maxima separated by a flat-topped throw profile.
330 F2 Fault (Set 1): the post-Early Messinian throw profile shows a bell-shaped geometry, with a
331 very pronounced peak in the central portion of the fault. The Early Messinian throw profile
332 does not show any displacement, whereas pre-Messinian throw profile displays both a flat-
333 topped geometry at ca. -200 m-throw along the NW edge, and a bell-shaped geometry, with a
334 peak at ca. 450 m-throw, along the SE edge.
335 F3 Fault (Set 3): the post-Early Messinian throw profile shows a bell-shaped geometry, with
336 two nearby maxima in the central portion of the fault. The Early Messinian throw profile
337 shows a slightly asymmetric geometry, with higher values towards the WSW edge of the
338 fault. The pre-Messinian throw profile displays a flat-topped geometry at around 100 m-
339 throw.
340 F4 Fault (Set 1): the post-Early Messinian throw profile shows an asymmetric shape, with the
341 greater values towards the NW edge of the fault. The Early Messinian throw profile does not
342 show any displacement, whereas the bottom pre-Messinian throw profile displays a slightly
343 pronounced, bell-shaped geometry towards the NW edge of the fault.
344 F5 Fault (Set 1): the post-Early Messinian throw profile shows a sort of asymmetric
345 geometry, with the greatest values localized at the NW edge of the fault. The Early Messinian
346 throw profile shows a flat-topped geometry, with values at ca. 100 m-throw. The pre-

Messinian throw profile displays two flat-topped geometries, localized at values of ca. 100 m. and -100 m-throw, respectively.

F6 Fault (Set 3): the post-Early Messinian throw profile forms a smooth, flat-topped geometry. Both Early Messinian and pre-Messinian throw profiles do not show any significant displacement.

F7 Fault (Set 3): the post-Early Messinian throw profile displays an asymmetric shape, with a maximum towards the WSW edge of the fault. The Early Messinian throw profile does not show any displacement, whereas the bottom pre-Messinian throw profile displays an asymmetric geometry characterized by two maxima localized at the fault tips.

F8 Fault (Set 3): the post-Early Messinian throw profile shows an asymmetric shape, with the greatest displacement localized at the WSW edge of the fault. The Early Messinian throw profile displays a very small amount of displacement, with a flat-topped geometry at ca. 70 m-throw. The pre-Messinian throw profile shows an asymmetric shape, with the greatest negative values towards the WSW edge of the fault.

F9 Fault (Set 1): the post-Early Messinian throw profile shows a bell-shaped geometry, with a maxima at around 100 m-throw. The Early Messinian throw profile shows a flat-topped geometry at around 60 m-throw. The pre-Messinian throw profile shows an asymmetric shape, with a maximum towards the SE edge of the fault.

F10 Fault (Set 4): all stratigraphic horizons display a flat-topped geometry, with a maximum of ca. 50 m-throw.

F11 Fault (Set 2): all stratigraphic horizons display a flat-topped geometry, with a maximum of ca. 90 m-throw (post-Early Messinian) and 50 m-throw (pre-Messinian and Early Messinian), respectively.

F12 Fault (Set 3): the post-Early Messinian throw profile shows a bell-shaped geometry, with a maximum at ca. 200 m-throw. The Early Messinian profile shows a flat-topped geometry

localized in the WSW portion of the fault at ca. 80 m-throw. The pre-Messinian profile displays a bell-shaped geometry, with negative values down to around -120 m-throw.

4.4 Fault scaling properties

Based upon the fault throw profiles shown above, the maximum computed vertical Displacement (D) - Length (L) data for the twelve faults (Table 2) that dissect the exposed Monte Alpi Unit are plotted in a log-log diagram (Figure 14a). As reported in the first section of the manuscript, the slope of the computed power law, best-fit line corresponds to the growth line of individual, isolated faults (Cartwright et al., 1995). As a result, a *n* value of ca. 1 is computed for the pre-Messinian faults. We note that a *n* value of ca. 0.8 is computed for the three faults active during Lower Messinian (Figure 14b), which is obviously not statistically significant due to the small number of data points (Massot et al., 2002). Differently, a *n* value of ca. 1.5 was computed for the post-Early Messinian fault growth line (Figure 14c). (insert Table 2 and Figure 14).

5. Data interpretation and discussion

5.1 Fault growth mechanisms

The most pronounced strike variations are computed for Set 1 Faults (Table 1). Assuming that these faults developed by mean of subsidiary, extensional faults localized at their releasing jogs and/or at the extensional quadrants of mode-II edges (Segall and Pollard, 1980, 1983; Mollema and Antonellini, 1999; Myers and Aydin, 2004; Flodin and Aydin, 2004; Agosta and Aydin, 2006; Antonellini et al., 2008; Agosta et al., 2010; Aydin et al., 2010), these variations could be due to either Early Pleistocene or Middle Pleistocene strike-slip tectonics. In fact, many authors assessed the occurrence of strike-slip along NW-SE striking faults exposed in the study area, and its surrounding regions, during Quaternary times (Knott 1987;

Carbone et al., 1991; Monaco and Tansi, 1992; Oldow et al., 1993; Monaco and Tortorici, 1998; Cello and Mazzoli, 1998; Tavarnelli and Pasqui, 2000; Van Dijk et al., 2000; Lentini et al., 2002; Mazzoli et al., 2006, 2014; La Bruna et al., 2017). Bearing the aforementioned interpretation in mind, the modalities of growth of the Monte Alpi extensional fault network are discussed hereafter by considering the computed fault throw profiles. Bell-shaped, flat-topped, and asymmetric cumulative fault throw profiles (Figure 12) indicate presence of isolated fault segments that likely interacted with each other during deformation (Muraoka and Kamata, 1983; Barnet et al., 1987; Walsh and Watterson, 1987, 1988, 1990; Peacock and Sanderson, 1991; Cowie and Scholz, 1992a; Cartwright et al., 1995; Huggings et al., 1995; Nicol et al., 1996; McLeod et al., 2000; Manighetti et al., 2001; Schlagenhauf et al., 2008).

A more detailed interpretation of the growth mechanisms can be deciphered by considering the pre-Messinian, Early Messinian, and post-Early Messinian fault throw profiles (Figure 13), and the results of stratigraphic field logging (Figure 8), Upper Messinian isopach map computation (Figure 9), and detailed field structural analyses (Figures 5 to 7). The pre-Messinian fault network was comprised of Sets 1, 2, and 3 faults, respectively striking NW-SE, NNW-SSE, and ENE-WSW. Among all the inferred syn-sedimentary Early Cretaceous faults, the greatest throw values were computed for Set 1 faults. The computed throw data for Sets 1 and 2 faults show that they were likely comprised of original, isolated fault segments, up to a few km-long, and characterized by bell-shaped throw profiles. The computed n value, ca. 1, indicates that these faults grew under constant driving stress conditions (Schultz et al., 2008), forming self-similar geometries (Mandelbrodt and Pignoni, 1983; Torabi and Berg, 2011). However, interaction and possible linkage processes (Walsh and Watterson, 1988) occurred among the isolated fault segments, as suggested by the wide data point dispersion (Figure 14a). Such a dispersion shifted the power law best fit line with respect to the theoretical fault growth line, traced according to the highest displacements values (Schultz et

al., 2010). Linkage processes took place in correspondence of stepover/relay zones (Trudgill and Cartwright, 1994; Fossen and Rotevatn, 2016), and determined lower D/L values for given fault lengths (Figure 14d). Then, displacement localization within the linkage zones due to enhanced shear stress (Aydin and Schultz, 1990) caused higher D/L values up to the theoretical fault growth line (Cowie and Scholz, 1992a,b; Cartwright et al., 1995; Mansfield and Cartwright, 1996).

Regarding the age of faulting, Sets 1 and 2 faults are ca. sub-parallel to those crosscutting the Outer Apulian Platform, and exposed at the Gargano Promontory and Murge Plateau of southern Italy (cf. inset of Figure 1). Since the latter faults were interpreted as Cretaceous structures (Bertotti, 2001; Korneva et al., 2014; Laurita et al., 2016; Petrullo et al., 2017; Vitale et al., 2017), a similar age is hence proposed for the study faults. In fact, these Sets 1 and 2 faults were likely coeval to the Set 3 faults, which strike ENE-WSW, documented along the western cliff of the Monte Alpi (Figures 5a and 5h).

The pre-Messinian, likely Early Cretaceous in age, fault system was re-activated during onset of the Monte Alpi foreland basin system, as suggested by both computed (Figure 13) and measured structural data (Figures 6a, h, i). This fault system included either isolated (*ie*. F5 and F12 faults), or interacting faults (*ie*. F3 Fault), which were characterized by flat-topped and asymmetric profiles, respectively. Focusing on post-Early Messinian times, all faults pertaining to the Monte Alpi network show evidences of slip. The computed *n* value is about 1.5 (Figure 14c). This value, which is significantly greater than those computed for both pre-Messinian and Early Messinian faults, is therefore consistent with a scale-dependent geometry of the post-early Messinian fault network (Watterson, 1986; Walsh and Watterson, 1988; Cowie and Scholz, 1992a,b; Scholz et al., 1993; Schlische et al., 1996; Kim and Sanderson, 2005; Schultz et al., 2008).

By considering both T- and Y-shaped intersections, we observe that the former geometry is

447 quite common in the modelled fault system (Figures 10, 14e). In fact, these types of
448 intersection characterize F6, F7 and F8 faults, which are bounded on both sides by the F4 and
449 F5 and the F5 and F8 faults, respectively. On the other hand, the bounding F4 and F5 faults
450 intersect southward the F3 fault also forming T-shaped intersections. Among these, we focus
451 on the detailed throw profile analysis of both F7 and F5 faults (Figure 14e), which downdrop
452 the same block but unfortunately do not show very significant evidences of mechanical
453 interaction (Walsh et al., 2003). Differently, the T-shaped intersection formed by both F5 and
454 F3 faults is characterized by a marked increases of vertical displacement in the zone where
455 the two fault footwalls coincide (Fig. 14e). Y-shaped intersections are investigated by
456 considering small (ca. 30°) and large (ca. 130°) alpha angles (Maerten et al., 1999). The
457 former case is displayed by the F11 Fault intersecting against the F4 Fault (Fig 14e). There, a
458 pronounced increase of vertical displacement occurs in the zone where the two fault footwalls
459 coincide (Fig. 13). The latter case if formed by the F12 Fault intersecting the F5 Fault (Fig.
460 14e), but the two fault throw profiles do not show any variation in coincidence of the
461 intersection line (Fig. 13).
462
463 *5.2 Implication for the evolution of the Messinian foreland basin system*
464 Results of the integrated field and laboratory analyses are consistent with a pre-Messinian
465 orthogonal fault system made up of isolated, interacting faults (Figure 15). During Early
466 Messinian times, with ongoing roll-back of the Apulian Platform (Royden et al., 1993;
467 Doglioni, 1999), shallow-water marine basins characterized by anoxic conditions (Taddei and
468 Siano, 1992) formed within the back-bulge deposition zone of the Inner Apulian Platform
469 (Patacca et al., 1992; Critelli et al., 2011; Vitale et al., 2012) or, alternatively, within outer
470 secondary basins (sensu Flemings and Jordan, 1989). According to both basin geometry and
471 infill, similar conclusions were proposed for the Sunda shelf region, Indonesia (Ben Avraham

472 and Emery, 1973), the Cordilleran foreland basin, USA (DeCelles and Burden, 1992; Plint et
473 al., 1993) and the Taranaki foreland basin, New Zealand (Holt and Stern, 1994). The Early
474 Messinian basin of Monte Alpi was mainly bounded by re-activated Set 1 (NW-SE) and Set 3
475 (ENE-WSW) faults. Activity of an orthogonal fault system during the earliest stages foreland
476 basin systems evolution was already documented by Tavani et al. (2015b) in the Prenestini
477 Mt. of central Apennines, Italy, and interpreted as due to along-foredeep stretching (Tavani et
478 al., 2015a). This process commonly takes place in correspondence of curved orogens
479 (Doglioni, 1995; Zhao and Jacobi, 1997; Whitaker and Engelder, 2006), such as the southern
480 Apennines FTB (Locardi, 1988).
481 Differently, the erosional surface topping the Early Messinian limestones possibly formed in
482 the forebulge (Figure 15), which is an area commonly characterized by a significant uplift
483 (DeCelles and Giles, 1996), and considered as a non-depositional and/or erosional zone
484 (Flemings and Jordan, 1989; Crampton and Allen, 1995). On the basis of the restored bottom
485 Late Messinian surface (Figure 6l), a structural horst bounded by Set 1 faults formed at that
486 time. This deformation caused emersion, and partial erosion, of both Mesozoic and Lower
487 Messinian carbonates. Subsequently, the stratigraphy of the Late Messinian deposit also
488 suggests that nucleation of the Monte Alpi foredeep basin was controlled by re-activation of
489 Set 3 faults (ENE-WSW), whereas as shown by the computed fault throw profiles its later
490 development was mainly due to activity of Set1 fault (NW-SE).
491 According to Walsh et al. (2002), we interpret that the steeper slope of the post-Early
492 Messinian fault growth line with respect to both pre-Messinian and Early Messinian lines
493 (Figures 14a to c) reflects the higher degree of maturity of the post-Early Messinian fault
494 network (Cartwright et al., 1995; Nicol et al., 1996; Gupta and Scholz, 2000), and/or the
495 pronounced lithostatic loading that occurred during post-Messinian times (Mazzoli et al.,
496 2006). Focusing on Late Messinian times, the foredeep basin was characterized by isolated

497 depocenters, in which up to 600 m-thick terrigenous sediments were deposited (Monaco et al.,
498 1998; cf. well 2 of Figure 2). Compared to the 1,000's m-thick Lower Pliocene (Casero, 2004;
499 Shiner et al., 2004) and Upper Pliocene-Lower Pleistocene foredeep infills (Balduzzi et al.,
500 1982, Casnedi, 1988a, b), the Late Messinian succession is interpreted as due to a first-order
501 stage of forebulge progradation (Catuneanu, 2004), which occurred during thrusting of the
502 outermost portions of the southern Apennines FTB (Marabini and Vai, 1985; Cavazza and
503 DeCelles, 1998; Vitale and Ciarcia, 2013). It can be therefore argued that the Messinian
504 foreland basin system of Monte Alpi developed during a rapid migration of the southern
505 Apennines FTB, which triggered a predominant elastic response to flexure of the Apulian
506 plate due to the low amount of its tectonic load (Crampton and Allen, 1995; DeCelles and
507 Giles, 1996; Catuneanu, 2004). (insert Figure 15).
508
509 **6. Conclusions**
510 The present work combined geological field mapping and stratigraphic logging with
511 subsurface seismic and well log data interpretation to perform the 3D geological
512 reconstruction of the Monte Alpi area, southern Italy. The goals were the assessment of both
513 growth mechanisms and scaling properties of the pre-Pliocene fault network, and the
514 understanding of the structural control played by high-angle extensional faults on the time-
515 space evolution of the Messinian foreland basin system. Field analyses were aimed at
516 assessing the stratigraphy of the Messinian mixed carbonate-terrigeneous deposits, and at
517 documenting Early Cretaceous, Early Messinian, and Late Messinian syn-sedimentary faults.
518 Seismic reflection profiles and well logs were interpreted in order to decipher the geometry of
519 the topmost surface of the Monte Alpi Unit. Results of both surface and subsurface analyses
520 were then input in Gocad® to perform the 3D geological reconstruction of the Monte Alpi
521 massif and its surrounding areas. This procedure was then followed by the computation of

Late Messinian isopach map, and of throw profiles for the individual structures forming the Monte Alpi fault network. Results after 3D geological modelling and throw profile analysis were discussed to assess its following time-dependent evolution:

- During pre-Messinian times, main NW-SE to NNW-SSE fault segments were active as isolated structures, which likely interacted and linked together during ongoing deformation. According to literature data, these faults likely formed during Early Cretaceous times within the Inner Apulian Platform. Field evidences also show minor ENE-WSW, Early Cretaceous, syn-sedimentary extensional faults. Dimensional properties computed for the NW-SE to NNW-SSE faults showed that these features formed as isolated faults within a network characterized by self-similar geometries.
- During Early Messinian time, most of the pre-existing NW-SE and ENE-WSW faults were re-activated in the back-bulge zone during the earliest stages of foreland basin system evolution. These faults bounded shallow-water marine basins, in which carbonate sediments were deposited under anoxic conditions. The computed dimensional properties are also consistent with a self-similar fault network.
- Subsequently, isolated structural horsts formed in the forebulge zone of the foreland basin system. The horsts were bounded by NW-SE faults, which caused uplift, tilting, and partial erosion of both Mesozoic and Lower Messinian carbonates.
- During Late Messinian times, a 100's m-deep foredeep basin characterized by half-graben depocenters bounded by NW-SE faults developed in the study area. Minor ENE-WSW faults were likely active during that time, forming a scale-dependent network in which the individual faults intersected the previously formed structures producing higher displacement/length values.

The complex tectonic evolution that affected the study area since Early Pliocene times profoundly modified the aforementioned structural configuration, and partially obliterated

547 the original fault network. However, the results presented in this work shed a new light
548 into the structural control exerted by inherited faults on the development of the Messinian
549 foreland basin system of Monte Alpi. Further analysis focused on the sedimentological
550 and petrographic characterization of the Messinian mixed carbonate-terrigeneous deposits
551 are required to better assess the geometry of the depositional environments, and their
552 relationships with the bounding high-angle faults.

553

554 **Acknowledgments**

555 The present work is part of the first author's Ph.D. Thesis Dissertation. Authors want to thank
556 Enrico Tavernelli and an anonymous reviewer for their advices and their helpful correction on
557 the paper manuscript. VLB acknowledges Stefano Mazzoli, Italo Sgrosso, Marcello
558 Schiattarella, Jean Borgomano, Sergio Longhitano and Carlos Pirmez for their thoughtful and
559 constructive discussions. The first author also acknowledges the great support provided by
560 Paola Castelluccio, Alessandro Giuffrida, Arturo La Bruna, Andrea Rustichelli, Anthony
561 Tendill, Christophe Matonti, and Sebastien Chatelée during field and laboratory analyses.
562 This work was supported by the Ministry of Education, University and Research (MIUR), and
563 by the Reservoir Characterization Project, a consortium of universities and energy companies
564 (www.rechproject.com). ENI is acknowledged for providing seismic reflection data pertaining
565 to the Monte Alpi and surrounding areas.

566

567

568 **References**

569 Agosta, F., Aydin, A., 2006. Architecture and deformation mechanism of a basin-bounding
570 normal fault in Mesozoic platform carbonates, central Italy. Journal of Structural
571 Geology 28, 1445-1467.
572 Agosta, F., Alessandroni, M., Tondi, E., Aydin A., 2010. Oblique normal faulting along the
573 northern edge of the Majella anticline, central Italy: Inferences on hydrocarbon migration
574 and accumulation. Journal of Structural Geology 32, 1317-1333.
575 Alberti, M., Lapenta, M.C., Maurella, A., 2001. New geological data on the basin units
576 surrounding the Monte Alpi unit (southern Italy). Bollettino della Società dei Naturalisti in
577 Napoli - Nuova Serie, 1, 85-96.
578 Antonellini, M., Tondi, E., Agosta, F., Aydin, A., Cello G., 2008. Failure modes in deep-
579 water carbonates and their impact for fault development: Majella Mountain, Central
580 Apennines, Italy. Marine and Petroleum Geology 25, 1074-1096.
581 Aydin, A., Schultz, R. A., 1990. Effect of mechanical interaction on the development of
582 strike-slip faults with echelon patterns. Journal of Structural Geology 12, 123-129.
583 Aydin, A., Antonellini, M., Tondi, E., Agosta F., 2010. Deformation along the leading edge
584 of the Maiella thrust sheet in central Italy. Journal of Structural Geology 32, 1291-1304.
585 Balduzzi, A., Casnedi, R., Crescenti, U., Mostardini, F., Tonna, M., 1982. Il Plio-Pleistocene
586 del sottosuolo del bacino lucano (Avanfossa appenninica). Geologica Romana 21, 1-28.
587 Barnett, J. A., Mortiner, J., Rippon, J. H., Walsh, J. J., Waternson, J., 1987. Displacement
588 geometry in the volume containing a single normal fault. AAPG Bullettin 71, 925-937.
589 Ben-Avraham, Z., Emery, K. O., 1973. Structural framework of Sunda shelf. AAPG Bulletin
590 57, 2323-2366.

591 Bertok, C., Martire, L., Perotti, E., d'Atri, A., Piana, F., 2012. Kilometre-scale
592 palaeoescarpements as evidevce for Cretaceous synsedimentary tectonics in the external
593 Briançonnais domain (Ligurian Alps, Italy). Sedimentary Geology 251-252, 58-75.
594 Bertotti, G., Picotti, V., Chilovi, C., Fantoni, R., Merlini, S., Mosconi, A. 2001. Neogene to
595 Quaternary sedimentary basins in the south Adriatic (Central Mediterranean): foredeeps
596 and lithospheric buckling. Tectonics 20, 771-787.
597 Boccaletti, M., Ciaranfi, N., Cosentino, D., Deiana, G., Gelati, R., Lentini, F., Tortorici, L.,
598 1990. Palinspastic restoration and paleogeographic reconstruction of the peri-Tyrrhenian
599 area during the Neogene. Palaeogeography, Palaeoclimatology, Palaeoecology 77, 41-50.
600 Bonardi, G., Ciarcia, S., Di Nocera, S., Matano, F., Sgrosso, I., Torre, M., 2009. Carta delle
601 principali unità cinematiche dell'Appennino meridionale. Nota illustrativa. Bollettino della
602 Società Geologica Italiana 128, 47-60.
603 Borgomano, J. R. F., 2000. The Upper Cretaceous carbonates of the Gargano-Murge region,
604 southern Italy: a model of platform-to-basin transition. AAPG bulletin 84, 1561-1588.
605 Butler, R.W.H., Mazzoli, S., Corrado, S., De Donatis, M., Scrocca, D., Di Bucci, D.,
606 Gambini, R., Naso, G., Nicolai, C., Shiner, P., Zucconi, V., 2004. Applying thick-skinned
607 tectonic models to the Apennine thrust belt of Italy – Limitations and implications. In:
608 Thrust tectonics and hydrocarbon systems (K.R. McClay, ed.). American Association of
609 Petroleum Geologists 82, 647-667.
610 Carbone, S., Catalano, S., Lentini, F., Monaco, C., 1988. Le unità stratigrafico-strutturali
611 dell'Alta Val d'Agri (Appennino lucano) nel quadro dell'evoluzione del sistema catena-
612 avanfossa. Memorie Società Geologica Italiana 41, 331-341.
613 Carbone, S., Lentini, F., 1990. Migrazione neogenica del sistema catena-avampaese
614 nell'Appennino meridionale: problematiche paleogeografiche e strutturali. Rivista Italiana
615 di Paleontologia e Stratigrafia 96, 271-296.

616 Carbone, S., Catalano, S., Lentini, F., Monaco, C., 1991. Carta geologica del bacino del fiume
617 Agri. Scala 1:50.000. Cartografia SELCA, Firenze.
618 Cartwright, J., Trudgill, B. D., Mansfield, C. S., 1995. Fault growth by segment linkage: an
619 explanation for scatter in maximum displacement and trace lenght data from Canyonlands
620 Graben of SE Utah. Journal of Structural Geology 17, 1319-1326.
621 Casero, P., 2004. Structural setting of petroleum exploration plays in Italy. Special volume of
622 the Italian Geological Society for the IGC 32, 189-199.
623 Casnedi, R., 1988a. La Fossa bradanica: origine, sedimentazione e migrazione. Memorie
624 Società Geologica Italiana 41, 439-448.
625 Casnedi, R., 1988b. Subsurface basin analysis of fault-controlled turbidite system in Bradano
626 trough, Southern Adriatic foredeep, Italy. AAPG Bulletin 72, 1370-1380.
627 Catalano, S., Monaco, C., Tortorici, L., Tansi, C., 1993. Pleistocene strike-slip tectonics in the
628 Lucanian Apennine (Southern Italy). Tectonics 12, 656-665.
629 Catuneanu, O., 2004. Retroarc foreland systems evolution through time. Journal of African
630 Earth Sciences 38, 225-242.
631 Caumon, G., Collon-Drouaillet, P., De Veslud, C. L. C., Viseur, S., Sausse, J., 2009. Surface-
632 based 3D modeling of geological structures. Mathematical Geosciences 41, 927-945.
633 Cavalcante, F., Belviso, C., Finizio, F., Lettino, A., Fiore, S., 2009. Carta geologica delle
634 Unità Liguridi dell'area del Pollino (Basilicata): Nuovi dati geologici, mineralogici e
635 petrografici. Digilabs, Bari, 36.
636 Cavazza, W., DeCelles, P. G., 1998. Upper Messinian siliciclastic rocks in southeastern
637 Calabria (southern Italy): palaeotectonic and eustatic implications for the evolution of the
638 central Mediterranean region. Tectonophysics 298, 223-241.
639 Cavazza, W., Roure, F., Ziegler, P., 2004. The Mediterranean Area and the Surrounding
640 Regions: Active Processes, Remnants of Former Tethyan Oceans and Related Thrust Belts.

In: W. Cavazza, F. Roure, W. Spakman, G.M. Stampfli and P Ziegler (Eds). The TRANSMED Atlas, 1-29.

Cello, G., Mazzoli, S., 1998. Apennine tectonics in southern Italy: a review. Journal of Geodynamics 27, 191-211.

Cowie, P. A., Scholz, C. H., 1992a. Physical explanation for the displacement-lenght relationship for faults using a post-yield fracture mechanics model. Journal of Structural Geology 14, 1133-1148.

Cowie, P. A., Scholz, C. H., 1992b. Displacement-length scaling relationships for fault: data synthesis and discussion. Journal of Structural Geology 14, 1149-1156.

Cowie, P. A., Roberts, G. P., 2001. Constraining slip rates and spacings for active normal faults. Journal of Structural Geology 23, 1901-1915.

Crampton, S. L., Allen, P. A., 1995. Recognition of forebulge unconformities associated with early stage foreland basin development: example from the North Alpine Foreland Basin. AAPG bulletin 79, 1495-1514.

Crider, J. G., Pollard, D. D., 1998. Fault linkage: Three-dimensional mechanical interaction between echelon normal faults. Journal of Geophysical Research: Solid Earth 103, 24373-24391.

Critelli, S., Muto, F., Perri, F., Tripodi, V., 2011. Relationships between lithospheric flexure, thrust tectonics and stratigraphic sequences in foreland setting: the southern Apennines foreland basin system, Italy. InTech Open Access Publisher 121-170.

D'Argenio, B., Pescatore, T., 1972. Schema geologico dell'Appennino Meridionale (Campania e Lucania). Atti del Conv. Moderne vedute sulla geologia dell'Appennino (Roma 16-18 Febbraio 1972). Accademia Nazionale dei Lincei 183, 49-72.

Dawers, N. H., Anders, M. H., 1995. Displacement-length scaling and fault linkage. Journal of Structural Geology 17, 607611-609614.

666 De Lorenzo, G., 1895. Osservazioni geologiche nell'Appennino della Basilicata meridionale.
667 Atti Accademia di Scienza Fisica. Materiali 27, 31.
668 Destro, N., 1995. Release fault: A variety of cross fault in linked extensional fault systems, in
669 the Sergipe-Alagoas Basin, NE Brazil. Journal of Structural Geology 17 615-629.
670 DeCelles, P. G., Burden, E. T., 1992. Non-marine sedimentation in the overfilled part of the
671 Jurassic-Cretaceous Cordilleran foreland basin: Morrison and Cloverly Formations, central
672 Wyoming, USA. Basin Research 4, 291-313.
673 DeCelles, P. G., Giles, K. A., 1996. Foreland basin systems. Basin research 8, 105-123.
674 Dewey, J. F., Helman, M. L., Turco, E., Hutton, D. H. W., Knott, S. D., 1989. Kinematics of
675 the western Mediterranean. In Coward M. P., Dietrich D., Park R. G., eds., Alpine
676 Tectonics. Geological Society of London Special Publication 45, 265-283.
677 Dix, C. H., 1955. Seismic velocities from surface measurements. Geophysics 20, 68-86.
678 Doglioni, C.,1991. A proposal for kynematic modeling of W-dipping subductions - Possible
679 applications to the Tyrrhenian-Apennines system. Terra Nova 3, 423-434.
680 Doglioni, C., 1995. Geological remarks on the relationships between extension and
681 convergent geodynamic settings. Tectonophysics 252, 253-267.
682 Doglioni, C., Gueguen, E., Harabaglia, P., Mongelli, F., 1999. On the origin of west-directed
683 subduction zones and applications to the western Mediterranean. Geological Society,
684 London, Special Publications 156, 541-561.
685 Dunham, R., 1962. Classification of Carbonate Rocks According to Depositional Textures. In
686 W.E. Ham, Classification of carbonate rocks. AAPG Memoir 1, 108-121.
687 Embry III, A. F., Klovan, J. E., 1971. A late Devonian reef tract on northeastern Banks Island,
688 NWT. Bulletin of Canadian Petroleum Geology 19, 730-781.
689 Festa, V., 2003. Cretaceous structural features of the Murge area (Apulian Foreland, southern
690 Italy). Eclogae Geological Helvetiae 96, 11-22.

691 Flemings, P. B., Jordan, T. E., 1989. A synthetic stratigraphic model of foreland basin
692 development. Journal of Geophysical Research: Solid Earth 94(B4), 3851-3866.
693 Flodin, E. A., Aydin, A., 2004. Evolution of a strike-slip fault network, Valley of Fire State
694 Park, southern Nevada. Geological Society of America Bulletin 116, 42-59.
695 Foglio I.G.M. 211, S. Arcangelo. Istituto Geografico Militare.
696 Fossen, H., Rotevatn, A., 2016. Fault linkage and relay structures in extensional settings-A
697 review. Earth-Science Reviews 154, 14-28.
698 Gawthorpe, R. L., Leeder, M. R., 2000. Tectono-sedimentary evolution of active extensional
699 basins. Basin Research 12, 195-218.
700 Ghisetti, F., Vezzani, L., 1981. Contribution of structural analysis to understanding the
701 geodynamic evolution of the Calabrian Arc (Southern Italy). Journal of Structural Geology 3,
702 371-381.
703 Ghisetti, F., Vezzani, L., 1997. Interfering paths of deformation and development of arcs in
704 the fold-and-thrust belt of central Apennines (Italy). Tectonics 16, 523-536.
705 Grandjacquet, C., 1963. Schéma structural de l'Apennin campano-lucanien (Italie). Revue de
706 Géographie Physique et de Géolgie Dynamique 25, 185-202.
707 Gupta, A., Scholz, C. H., 2000. A model of normal fault interaction based on observations
708 and theory. Journal of Structural Geology 22, 865-879.
709 Harding, T. P., Tuminas, A. C., 1989. Structural interpretation of hydrocarbon traps sealed by
710 basement normal block faults at stable flank of foredeep basins and at rift basins. AAPG
711 Bulletin 73, 812-840.
712 Holt, W. E., Stern, T. A., 1994. Subduction, platform subsidence, and foreland thrust loading:
713 The late Tertiary development of Taranaki Basin, New Zealand. Tectonics 13, 1068-1092.

714 Huggins, P., Watterson, J., Walsh, J. J., Childs, C., 1995. Relay zone geometry and
715 displacement transfer between normal faults recorded in coal-mine plans. Journal of
716 Structural Geology 17, 1741-1755.
717 Improta, L., Iannaccone, G., Capuano, P., Zollo, A., Scandone, P., 2000. Inferences on the
718 upper crustal structure of Southern Apennines (Italy) from seismic refraction investigations
719 and sub-surface data. Tectonophysics 317, 273-297.
720 Ippolito, F., D'Argenio, B., Pescatore, T., Scandone, P., 1975. Structural-stratigraphic units
721 and tectonic framework of Southern Apennines. In SQUYRES C. Ed., Geology of Italy,
722 Earth Science. Society of Lybian Arabic Republic 317-328.
723 Kim, Y.S., Sanderson, D. J., 2005. The relationship between displacement and length of
724 faults. Earth Science Reviews 68, 317-334.
725 Knott, S. D., 1987. The Liguride Complex of southern Italy-a Cretaceous to Paleogene
726 accretionary wedge. Tectonophysics 142, 217-226.
727 Korneva, I., Tondi, E., Agosta, F., Rustichelli, A., Spina, V., Bitonte, R., Di Cuia, R., 2014.
728 Structural properties of fractured and faulted Cretaceous platform carbonates, Murge
729 Plateau (southern Italy). Marine and Petroleum Geology 57, 312-326.
730 La Bruna, V., Agosta, F., Prosser, G., 2017. New insights on the structural setting of the
731 Monte Alpi area, Basilicata, Italy. Italian Journal of Geosciences. 136, 220-237.
732 Laurita, S., Agosta, F., Cavalcante, F., Rustichelli, A., Giorgioni, M., 2016. Shearing of syn-
733 sedimentary carbonate breccia along strike-slip faults, Altamura Fm., Southern
734 Italy. Italian Journal of Geosciences 135, 41-54.
735 Lentini, F.,1991. Carta geologica del Bacino del Fiume Agri. Regione Basilicata-
736 Dipartimento Assetto del Territorio. S.EL.CA., Firenze

737 Lentini, F., Carbone, S., Catalano, S., Monaco, C., 2002. Confronti sedimentologico-
738 petrografici e posizione strutturale dei flysch di Albidona e di Gorgoglione nella media val
739 d'Agri (Appennino lucano). Memorie della Società Geologica Italiana 38, 259-273.
740 Locardi, E., 1988. The origin of the Apennine Arcs. Tectonophysics 146, 105-123.
741 Lorenzo, J. M., O'Brien, G. W., Stewart, J., Tandon, K., 1998. Inelastic yielding and
742 forebulge shape across a modern foreland basin: North West Shelf of Australia, Timor Sea.
743 Geophysical Research Letters 25, 1455-1458.
744 Maerten, L., Willemse, E. J., Pollard, D. D., Rawnsley, K., 1999. Slip distributions on
745 intersecting normal faults. Journal of Structural Geology 21, 259-272.
746 Mallet, J. L., Jacquemin, P., Cheimanoff, N., 1989. GOCAD project: Geometric modeling of
747 complex geological surfaces, In SEG Technical Program Expanded Abstracts 1989.
748 Society of Exploration Geophysicists 126-128.
749 Mallet, J. L., 2002. Geomodeling *Oxford University Press*.
750 Mandelbrot, B. B., Pignoni, R., 1983. The fractal geometry of nature (Vol. 173). New York:
751 WH freeman.
752 Manighetti, I., King, G. C. P., Gaudemer, Y., Scholz, C. H., Doubre, C., 2001. Slip
753 accumulation and lateral propagation of active normal faults in Afar. Journal of
754 Geophysical Research: Solid Earth 106, 13667-13696.
755 Mansfield, C. S., Cartwright, J. A., 1996. High resolution fault displacement mapping from
756 three-dimensional seismic data: evidence for dip linkage during fault growth. Journal of
757 Structural Geology 18, 249-263.
758 Marabini, S., Vai, G. B., 1985. Analisi di facies e macrotettonica della vena del gesso di
759 Romagna. Bollettino della Società Geologica Italiana 104, 21-42.
760 Massot, J., 2002. Implementation of 3D balanced restoration methods. Ph.D. Dissertation.
761 Institut Polytechnique National de Lorraine, Nancy, France, 157 pp.

762 Mazzoli, S., Aldega, L., Corrado, S., Invernizzi, C., Zattin, M., 2006. Pliocene-Quaternary
763 thrusting, syn-orogenic extension and tectonic exhumation in the southern Apennines
764 (Italy): Insights from the Alpi Mt. area. In Styles of Continental Contraction, edited by S.
765 Mazzoli and R.W.H. Butler. Geological Society of America 414, 55-77.
766 Mazzoli, S., Ascione, A., Buscher, J. T, Pignalosa. A., Valente, E., Zattin, M., 2014. Low-
767 angle normal faulting and focused exhumation associated with late Pliocene change in
768 tectonic style in the southern Apennines (Italy). Tectonics 33,1802-1818.
769 McLeod, A., Dawers, N. H., Underhill, J. R., 2000. The propagation and linkage of normal
770 faults: insight from the Strathspey-Brent-Statfjord fault array, northern North Sea. Basin
771 Research 12, 263-284.
772 Medwedeff, D. A., Krantz, R. W., 2002. Kinematic and long modelling of 3-D extensional
773 ramps: observations and a new 3-D deformation model. Journal of Structural Geology 24
774 763-772.
775 Menardi Noguera, A., Rea, G., 2000. Deep structure of the Campanian-Lucanian Arc
776 (southern Apennines). Tectonophysics 324, 239-265.
777 Meyer, V., Nicol, A., Childs, C., Walsh, J. J., Watterson, J., 2002. Progressive localisation of
778 strain during the evolution of a normal fault population. Journal of Structural Geology 24,
779 1215-1231.
780 Monaco, C., Tansi, C., 1992. Strutture transpressive lungo la zona trascorrente sinistra nel
781 versante orientale del Pollino (Appennino calabro-lucano). Bollettino della Società
782 Geologica Italiana 111, 291-301.
783 Monaco, C., Tortorici, L. 1995). Tectonic role of ophiolitic-bearing terranes in the
784 development of the Southern Apennine orogenic belt. Terra Nova 7, 153-160.
785 Monaco, C., Tortorici, L. Paltrinieri, W., 1998. Structural evolution of the Lucanian
786 Apennines, southern Italy. Journal of Structural Geology 20, 617-638.

787 Molemma, P. N., Antonellini, M., 1999. Development of strike-slip faults in the Dolomites of
788 the Sella Group, Northern Italy. Journal of Structural Geology 21, 273-292.
789 Mostardini, F., Merlini, S., 1986. Appennino centro-meridionale. Sezioni geologiche e
790 proposta di modello strutturale. Memorie della Società Geologica Italiana 35, 177-202.
791 Muller, C., Casero, P., Moretti, I., Roure, F., Sage, L., 1988. Significance of the Alpi Mt. in
792 the geodynamic evolution of the Southern Apennines. Atti 74th Congresso della Società
793 Geologica Italiana B, 333-335.
794 Muraoka, H., Kamata, H., 1983. Displacement distribution along minor fault traces. Journal
795 of Structural Geology 5, 483-495.
796 Myers, R., Aydin A., 2004. The evolution of faults formed by shearing across joint zones in
797 sandstones. Journal of Structural Geology 26, 947-966.
798 Nicol, A., Watterson, J., Walsh, J. J., Childs, C., 1996. The shapes, major axis orientations
799 and displacement patterns of fault surfaces. Journal of Structural Geology 18, 235-248.
800 Nicolai, C., Gambini, R., 2007. Structural architecture of the Adria platform-and-basin
801 system. Bollettino Società Geologica Italiana 7, 21-37.
802 Ogniben, L., 1969. Schema introduttivo alla geologia del confine calabro-lucano. Memorie
803 della Società Geologica Italiana 8, 453-763.
804 Oldow, J. S., D'Argenio, B., Ferranti, L., Pappone, G., Marsella, E., Sacchi, M., 1993. Large-
805 scale longitudinal extension in the southern Apennines contractional belt, Italy. Geology
806 21, 1123-1126
807 Ortolani, F., Torre, M., 1971. Il Mt. Alpi (Lucania) nella paleogeografia dell'Appennino
808 meridionale. Bollettino della Società Geologica Italiana 90, 213-248.
809 Panza, E., Agosta, F., Zambrano, M., Tondi, E., Prosser, G., Giorgioni, M., Janiseck, J. M.,
810 2015. Structural architecture and Discrete Fracture Network modelling of layered fractured
811 carbonates (Altamura Fm., Italy). Italian Journal of Geosciences 134, 409-422.

812 Panza, E., Agosta, F., Zambrano, M., Tondi, E., Prosser, G., Giorgioni, M., Janiseck, J. M.,
813 2016. Fracture stratigraphy and fluid flow properties of shallow-water, tight carbonates:
814 The case study of the Murge Plateau (southern Italy). Marine and Petroleum Geology 73,
815 350-370.
816 Patacca, E., Sartori, R., Scandone, P. 1990. Tyrrhenian basin and Apenninic arcs: kinematic
817 relations since late Tortonian times. Memorie Società Geologica Italiana 45, 425-451.
818 Patacca, E., Scandone, P., Bellatalla, M., Perilli, N., Santini, U., 1992. The Numidian-sand
819 event in the Southern Apennines. Mem. Sci. Geol. Padova 43, 297-337.
820 Patacca, E., Scandone, P., 2007. Geology of southern Apennines. Results of the CROP
821 Project. Sub-project CROP-04: In: Mazzotti A., Patacca E., Scandone P., (Eds). Bollettino
822 della Società Geologica Italiana 7, 75-119.
823 Peacock, D.C.P., Sanderson, D. J., 1991. Displacement, segment linkage and relay ramps in
824 normal fault zones. Journal of Structural Geology 13, 721-733.
825 Pescatore, T., Renda, P., Schiattarella, M., Tramutoli, M., 1999. Stratigraphic and structural
826 relationships between Meso-Cenozoic Lagonegro basin and coeval carbonate platforms in
827 southern Apennines, Italy. Tectonophysics 315, 269-286.
828 Petrullo, A. V., Agosta, F., Prosser, G., Rizzo, E., 2017. Cenozoic tectonic evolution of the
829 northern Apulian carbonate platform (southern Italy). Italian Journal of Geosciences 136,
830 296-311.
831 Pieri, P., Laviano A., 1989. Tettonica e sedimentazione nei depositi senomiani delle Murge
832 sud-orientali (Ostuni). Bollettino della Società Geologica Italiana 108, 351-356.
833 Pieri, P., Festa, V., Moretti, M., Tropeano, M., 1997. Quaternary tectonic activity of the
834 Murge area (Apulian foreland-Southern Italy). Annals of Geophysics 40.

835 Plint, A. G., Hart, B. S., Donaldson, W. S., 1993. Lithospheric flexure as a control on stratal
836 geometry and facies distribution in Upper Cretaceous rocks of the Alberta foreland basin.
837 Basin Research 5, 69-77.
838 Ranero, C.R., Morgan, J.P., McIntosh, K., Reichert, C., 2003. Bending-related faulting and
839 mantle serpentinization at the Middle America trench. Nature 425, 36-373.
840 Roda, C., 1965. Livelli a struttura grumosa e livelli ad ooliti rotte e rigenerate nel calcare
841 miocenico del Alpi Mt. (Potenza). Geologica Romana 4.
842 Royden, L., Patacca, E., Scandone, P., 1987. Segmentation and configuration of subducted
843 lithosphere in Italy: An important control on thrust-belt and foredeep-basin evolution.
844 Geology 15, 714-717.
845 Royden, L. H., 1993. The tectonic expression slab pull at continental convergent boundaries.
846 Tectonics 12, 303-325.
847 Sartoni, S., Crescenti U., 1962. Ricerche biostratigrafiche nel Mesozoico dell'Appennino
848 Meridionale. Giornale di Geologia 29, 161-309.
849 Schettino, A., Turco E., 2011. Tectonic history of the western Tethys since the late Triassic.
850 Geological Society of America Bulletin 123, 89–105.
851 Shiner, P., Beccacini, A., Mazzoli, S., 2004. Thin-skinned versus thick-skinned structural
852 models for Apulian Carbonate Reservoirs: constraints from the Val D'Agri Field. Marine
853 and Petroleum Geology 21, 805-827.
854 Schlagenhauf, A., Manighetti, I., Malavieille, J., Dominguez, S., 2008. Incremental growth of
855 normal faults: Insights from a laser-equipped analog experiment. Earth and Planetary
856 Science Letters 273, 299-311.
857 Schlische, R. W., Young, S. S., Ackermann, R. V, Gupta, A., 1996. Geometry and scaling
858 relations of a population of very small rift-related normal faults. Geology 24, 683-686.

859 Scholz, C. H., Dawers N. H., Yu, J. Z., Anders, M. H., Cowie, P. A., 1993. Fault growth and
860 fault scaling laws: preliminary results. Journal of Geophysical Research: Solid Earth 98,
861 21951-21961.
862 Schultz, R. A., Soliva, R., Fossen, H., Okubo, C. H., Reeves, D. M., 2008. Dependence of
863 displacement–length scaling relations for fractures and deformation bands on the
864 volumetric changes across them. Journal of Structural Geology 30, 1405-1411.
865 Schultz, R. A., Soliva, R., Okubo, C. H., Mege, D., 2010. Fault populations. Planetary
866 Tectonics 457-510.
867 Segall, P., Pollard D. D., 1980. Mechanics of discontinuous faults. Journal of Geophysical
868 Research: Solid Earth 85, 4337-4350.
869 Segall, P., Pollard, D. D., 1983. Nucleation and growth of strike slip faults in granite. Journal
870 of Geophysical Research: Solid Earth 88, 555-568
871 Selli, R., 1957. Sulla trasgressione del Miocene nell'Italia meridionale. Giornale Di Geologia
872 2, 26-54.
873 Sgrosso, I., 1988. Nuovi dati biostratigrafici sul Miocene del M. Alpi (Lucania) e conseguenti
874 ipotesi paleogeografiche. Memorie della Società Geologica Italiana 41, 343-351.
875 Spalluto, L., 2012. Facies evolution and sequence chronostratigraphy of a "mid"-Cretaceous
876 shallow-water carbonate succession of the Apulia Carbonate Platform from the northern
877 Murge area (Apulia, southern Italy). Facies 58, 17-36.
878 Taddei, A., Siano, M. G., 1992. Analisi biostratigrafica e considerazioni paleoecologiche sulla
879 successione neogenica del Alpi Mt. (Lucania). Bollettino della Società Geologica Italiana
880 111, 255-272.
881 Tavani, S., Carola E., Granado, P., Quintà, A., Muñoz, J. A., 2013. Transpressive inversion of
882 a Mesozoic extensional forced fold system with an intermediate décollement level in the
883 Basque-Cantabrian Basin (Spain). Tectonics 32, 146-158.

884 Tavani, S., Storti. F., Lacombe, O., Corradetti, A., Muñoz, J. A. Mazzoli, S., 2015a. A review
885 of deformation pattern templates in foreland basin systems and fold-and-thrust belts:
886 Implications for the state of stress in the frontal regions of thrust wedges. Earth Sciences
887 Reviews 141, 82-104.
888 Tavani, S., Vignaroli, G., Parente, M., 2015b. Transverse versus longitudinal extension in the
889 foredeep-peripheral bulge system: Role of Cretaceous structural inheritances during early
890 Miocene extensional faulting in inner central Apennines belt. Tectonics 34, 1412-1430.
891 Tavarnelli, E., Decandia, F.A., Alberti A., 1999. Evidenze di tettonica distensiva
892 sinsedimentaria nel Bacino messiniano della Laga:implicazioni per l'evoluzione
893 dell'Appennino Settentrionale. Bollettino della Società Geologica Italiana, 118, 2, 217-
894 227.
895 Tavarnelli, E., Pasqui, V., 2000. Fault growth by segment linkage in seismically active
896 settings: examples from the Southern Apennnines, Italy, and the Coast Ranges, California.
897 Journal of Geodynamics, 29, 501-516.
898 Tavarnelli, E., Prosser, G., 2003. The complete Apennines orogenic cycle preserved in a
899 transient single outcrop near San Fele, Lucania, Southern Italy. Journal of the Geological
900 Society of London, 160, 429-434.
901 Torabi, A., Berg, S. S., 2011. Scaling of fault attributes: A review. Marine and Petroleum
902 Geology 28, 1444-1460.
903 Trudgill, B., Cartwright, J., 1994. Relay-ramp forms and normal-fault linkages, Canyonlands
904 National Park, Utah. Geological Society of America Bulletin 106, 1143-1157.
905 Vai, G.B., Martini, I. P., 2001. Basament and early (pre-Alpine) history. In Vai, G. B.,
906 Martini, I. P., Eds., Anatomy of an Orogen: The Apennines and Adjacent Mediterranean
907 Basins. Kluwer Academic Publication 121-150.

908 Van Dijk, J. P., Okkes, F. W. M., 1990. The analysis of shear zones in Calabria: implications
909 for the geodynamics of the Central Mediterranean. Rivista Italiana di Paleontolologia e
910 Stratigrafia 96, 241-270.
911 Van Dijk, J. P., Bello, M., Toscano, C., Bersani, A., Nardon, S., 2000. Tectonic model and
912 three-dimensional fracture network analysis of Alpi Mt. (southern Apennines).
913 Tectonophysics 324, 203-237.
914 Vitale, S., Dati, F., Mazzoli, S., Ciarcia, S., Guerriero, V., Iannace, A. 2012. Modes and
915 timing of fracture network development in poly-deformed carbonate reservoir analogues,
916 Mt. Chianello, southern Italy. Journal of Structural Geology 37, 223-235.
917 Vitale, S., Ciarcia, S., 2013. Tectono-stratigraphic and kinematic evolution of the
918 southern Apennines/Calabria–Peloritani Terrane system (Italy). Tectonophysics 583, 164-
919 182.
920 Vitale, S., Amore, O. F., Ciarcia, S., Fedele, L., Grifa, C., Prinzi, E. P., Tavani, S.,
921 Tramparulo, F. D. A., 2017. Structural, stratigraphic, and petrological clues for a
922 Cretaceous–Paleogene abortive rift in the southern Adria domain (southern Apennines,
923 Italy). Geological Journal DOI: 10.1002/gj.2919.
924 Walsh, J. J., Watterson, J., 1987. Distributions of cumulative displacement and seismic slip on
925 a single normal fault surface. Journal of Structural Geology 9(8), 1039-1046.
926 Walsh, J. J., Watterson, J., 1988. Analysis of the relationship between displacements and
927 dimensions of faults. Journal of Structural Geology 10, 239-247.
928 Walsh, J. J., Watterson, J., 1990. New methods of fault projection for coalmine planning.
929 Proceedings of the Yorkshire Geological Society 48, 209-219.
930 Walsh, J. J., Nicol, A., Childs, C., 2002. An alternative model for the growth of faults. Journal
931 of Structural Geology 24, 1669-1675.

Walsh, J. J., Bailey, W. R., Childs, C., Nicol, A., Bonson, C. G., 2003. Formation of segmented normal faults: a 3-D perspective. Journal of Structural Geology 25, 1251-1262.

Watterson, J., 1986. Fault dimensions, displacements and growth. Pure and Applied Geophysics 124(1-2), 365-373.

Whitaker, A. E., Engelder, T., 2006. Plate-scale stress fields driving the tectonic evolution of the central Ouachita salient, Oklahoma and Arkansas. Geological Society of America Bulletin 118, 710-723.

Zhao, M., Jacobi, R. D., 1997. Formation of regional cross-fold joints in the northern Appalachian Plateau. Journal of Structural Geology 19, 817-834.

Figure caption

Figure 1. Simplified geological map of the Southern Apennines, Italy, and NE-SW geological cross section (from *Vitale and Ciarcia*, 2013, and references therein). Location of the study area of Monte Alpi is shown both in the geological map and in the inset figure.

Figure 2. (**a**) Geological map of the Monte Alpi area, and surrounding regions, at a 1:25.000 scale. Data after original field survey and available bibliograpy (*Foglio IGM 211, S. Arcangelo; Bonardi et al.,* 2009*; Cavalcante et al.,* 2009; *Lentini,* 1991). (**b**) Location of the sites of stratigraphic logging analysis; (**c**) Traces of the main faults pertaining to the Monte Alpi structural network.

Figure 3. Original and interpreted seismic reflection profiles available for the study area. Traces of individual seismic profiles are reported in Figure 2. Interpreted sections show the main structural features crosscutting the Apulian Platform and allochthonous units. Interpretation of stratigraphic horizons and both low-angle and high-angle faults are based on available well log data.

Figure 4. (**a**) Modelled fault surface view due to west. Grey lines represent points with similar amounts of throw present along the fault surface, whereas dashed lines show the cut-off of the bottom Lower-Cretaceous, Early Messinian and Late Messinian surfaces. (**b**)Throw profile computational process on the F1 Fault.

Figure 5. (a) Panoramic view of the western edge of Monte Alpi. There, Mesozoic platform carbonates are overlain by two Messinian sedimentary intervals. The lower interval is made up of ramp limestones, whereas the upper one includes shallow-marine siliclastics. (**b to g**) Photomicrographs of representative samples of the Mesozoic platform carbonates. (**h, i**) Outcrop view of a portion of the Monte Alpi western cliff, along which a ENE-WSW striking, Early Cretaceous, syn-sedimentary normal fault is exposed.

971
972 **Figure 6.** (**a**) Panoramic view of the western edge of the Monte Santa Croce peak (cf. Figure
973 2). (**b to g**) Photomicrographs of representative samples of the Lower Messinian carbonates.
974 (**h and i**) Outcrop view and line-drawing of a ENE-WSW striking, Early Messinian, syn-
975 sedimentary normal fault.
976
977 **Figure 7.** (**a**) Outcrop view of the Solarino site (western edge of Monte Alpi). There, the
978 Upper Messinian conglomerates form an onlap geometry with respect to the NNW-SSE
979 striking F11 Fault, which is therefore interpreted as Late Messinian in age. (**b**) North-eastern
980 edge of the Monte Santa Croce Peak (cf. Figure 2). There, the Upper Messinian sandstones
981 and conglomerates form a down-lap geometry with respect to the erosional surface topping
982 the Lower Messinian carbonates. (**c**) Close up view of the Solarino site, where flattened-
983 polygenic conglomerates pertaining to the Upper Messinian deposit are exposed. (**d**) outcrop
984 view of the Canale del Grillone site (western sector), where Upper Messinian laminated
985 sandstones crop out.
986
987 **Figure 8.** Stratigraphic logs measured across the exposed sections of the Messinian mixed
988 carbonates/terrigenous deposits. The location of each log is reported in Figure 2.
989
990 **Figure 9.** (**a**) Isopach map computed for the Upper Messinian terrigenous deposit. Data are
991 reported in meters. White lines represent the traces of the modelled Monte Alpi simplified
992 fault network. (**b**) Lower hemisphere, equal area projections of both poles and planes related
993 to unrestored and restored bottom Late Messinian surfaces. Bedding plane data were gathered
994 in the field from both western (Canale del Grillone) and eastern (Santa Croce) sectors of
995 Monte Alpi. The cartoons show the unrestored and restored geological cross-sections
996 elaborated for the study area. Data were restored according to the attitude of Upper Messinian
997 beds.
998
999 **Figure 10.** (**a**) Simplified traces of the Monte Alpi fault network. Dashed lines represent the
1000 traces of blind faults. Blue labels are assigned to the faults that are used for throw analysis.
1001 (**b**) Histograms showing both azimuth and dip variations computed for the F1 Fault surface.
1002 Both histograms describe the mean of the azimuth/dip value. (**c**) Snapshot of the 3D
1003 geological reconstruction, where the bottom Early Cretaceous surface, F1 Fault, and original
1004 geological map are shown.
1005
1006 **Figure 11.** (**a**) Outcrop view of the N-S striking F1 Fault, which bounds the north-western
1007 edge of Monte Alpi. The fault crosscut Jurassic carbonates, and it is characterized by both
1008 dip-slip and oblique-slip, extensional kinematics. (**b**, **c**) Close up of the F1 Fault. Kinematic
1009 indicators, such as calcite fibers and abrasion striae, are visible along the main slip surface.
1010 (**d**) E-W striking, F3 Fault juxtaposing the Monte La Spina dolostones against Lower
1011 Cretaceous carbonate. The inset shows the polished slickenside, in which with dip-slip striae
1012 are visible. (**e**) Outcrop view of the F10 fault, which crosscut Lower Messinian carbonates.
1013 The inset shows the small veneer of cataclasites present along the polished slickenside;
1014
1015 **Figure 12.** Cumulative throw profiles computed for the 12 major faults pertaining to the
1016 Monte Alpi network, in which are present faults with different shape regarding the computed
1017 throw profiles (symmetric, bell-shaped, flat-topped and asymmetric profiles). See text for
1018 explanation.
1019

Figure 13. Pre-Messinian (blue), Early Messinian (green), and post-Early Messinian (yellow) throw profiles computed for the 12 major faults pertaining to the Monte Alpi network. See text for explanation.

Figure 14. Log-Log plots of displacement vs. length data computed for (**a**) pre-Messinian faults ($y=0.07x^{0.9}$; $R^2=0.42$), (**b**) Early Messinian faults ($y=0.06x^{0.8}$; $R^2=0.86$), and (**c**) post-Early Messinian faults ($y=0.08x^{1.5}$; $R^2=0.71$). (**d**) Cartoons showing the main stages of fault growth, and their related log displacement/ log length data, according to *Cartwright et al.* (1995). (**e**) Cartoons showing both T and Y-shaped intersections for some of the studied faults.

Figure 15. Time/space evolutionary model proposed for the Monte Alpi foreland basin system. The faults active during the main tectonic stages are illustrated in the 3D block diagrams, in which the geometry of the sedimentary depocenters is also reported.

Table 1. Results of fault analysis performed on the 27 faults used for the 3D geological reconstruction. The 75, 50, and 25 percentile distributions of both dip azimuth and dip angle computed for the individual faults are shown, respectively. The two main clusters of dip azimuth values are computed on the basis of the obtained histograms (ie. Figure 10b), in order to decipher the possible horizontal veering of the modelled 3D fault surfaces. In fact, the amount of strike variation reported in the last column is related to the difference between the two clusters computed, along a horizontal plane, for each modelled fault.

Table 2. Name, length and vertical throw of the computed fault segments related to the Pre-Messinian (blue), Early Messinian (green), and post-Early Messinian (yellow) structural network.

Figure 6. (**a**) Panoramic view of the western edge of the Monte Santa Croce peak (cf. Figure 2). (**b to g**) Photomicrographs of representative samples of the Lower Messinian carbonates. (**h and i**) Outcrop view and line-drawing of a ENE-WSW striking, Early Messinian, syn-sedimentary normal fault.

NAME	SET	DIP AZIMUTH 75%	DIP AZIMUTH 50%	DIP AZIMUTH 25%	DIP ANGLE 75%	DIP ANGLE 50%	DIP ANGLE 25%	DIP AZIMUTH CLUSTER 1	DIP AZIMUTH CLUSTER 2	STRIKE VARIATION
F1	II	254.1	248.6	237.9	88.5	85.1	80.7	254	75	1°
F2	I	234.7	194.4	35.7	88.9	87.4	85	235	35	20°
F3	III	319.3	315.9	191.7	86.1	83.5	78.8	320	135	5°
F4	I	228.4	58.5	52.4	88	84.4	75.4	225	60	15°
F5	I	223.5	202.2	42.8	89	87.6	85.4	235	40	15°
F6	III	342	336.5	323	77.6	74.1	69.2	345	/	/
F7	III	159.1	157.2	155.5	79.8	73.5	67.9	/	/	/
F8	III	155.3	155.1	154.9	89.1	88.3	87.9	/	/	/
F9	I	38.6	29.3	25.5	68.1	65.4	64.1	/	/	/
F10	IV	203.1	23.3	22.5	89.6	89.3	87.6	204	23	1°
F11	II	76.9	74.1	70	87.4	85.6	81.5	70	260	10°
F12	III	344.8	188.9	180.4	87.3	83.6	81.5	170	345	5°
F13	I	228.6	227.5	223.5	87.5	86.1	84.4	/	/	/
F14	V	187	12.7	8.6	89	88.3	87.5	180	8	8°
F15	IV	97.1	89.4	76.5	61.4	59	55.7	/	/	/
F16	IV	107.2	92.8	77.3	65.8	64	62.7	/	/	/
F17	II	76.2	72.5	68.9	74.2	67.7	62.3	/	/	/
F18	II	75.9	70.5	66.9	71.7	64.4	58.8	/	/	/
F19	I	226.1	225.1	224	78.2	77.4	75.6	/	/	/
F20	V	112.2	109.3	108.1	79.6	78.6	76.8	/	/	/
F21	V	19.7	17.9	13.8	73.9	72.2	71.1	/	/	/
F22	III	325.7	319.8	307.3	85.3	81.5	77.5	/	/	/
F23	II	251.4	249.7	245.8	87.5	86.8	85.9	/	/	/
F24	IV	193	249.7	12.7	88.2	86.7	84.2	193	20	7°
F25	IV	104.9	103.3	102.7	87.7	86.7	86	/	/	/
F26	III	344.5	14.4	10.6	87	83.7	78.3	/	/	/
F27	L.A.N.F.	135.2	86.3	53.6	25.5	22.4	18	/	/	/

	NAME	LENGTH (km)	VERTICAL FAULT THROW (km)
P.M.	F1a	4	0,5
	F1b	3,5	0,6
	F2a	4,2	0,2
	F2b	3,5	0,45
	F3	4	0,15
	F4	1,5	0,05
	F5a	2	0,1
	F5b	1,5	0,08
	F7a	0,6	0,1
	F7b	0,6	0,15
	F8	1,5	0,07
	F9	2,5	0,25
	F10	1	0,02
	F11	1	0,02
	F12	1	0,1
E.M.	F3	1,5	0,1
	F5	4	0,15
	F12	1	0,05
P.E.M.	F1	6,2	0,9
	F2a	3	0,6
	F2b	4	1,4
	F2c	2	0,25
	F3	4,5	0,8
	F4	4,8	0,5
	F5	4	0,5
	F6	1,2	0,2
	F7	1	0,25
	F8	1,8	0,16
	F9	3	0,15
	F10	1	0,02
	F11a	0,6	0,02
	F11b	0,8	0,07
	F12	1,6	0,2

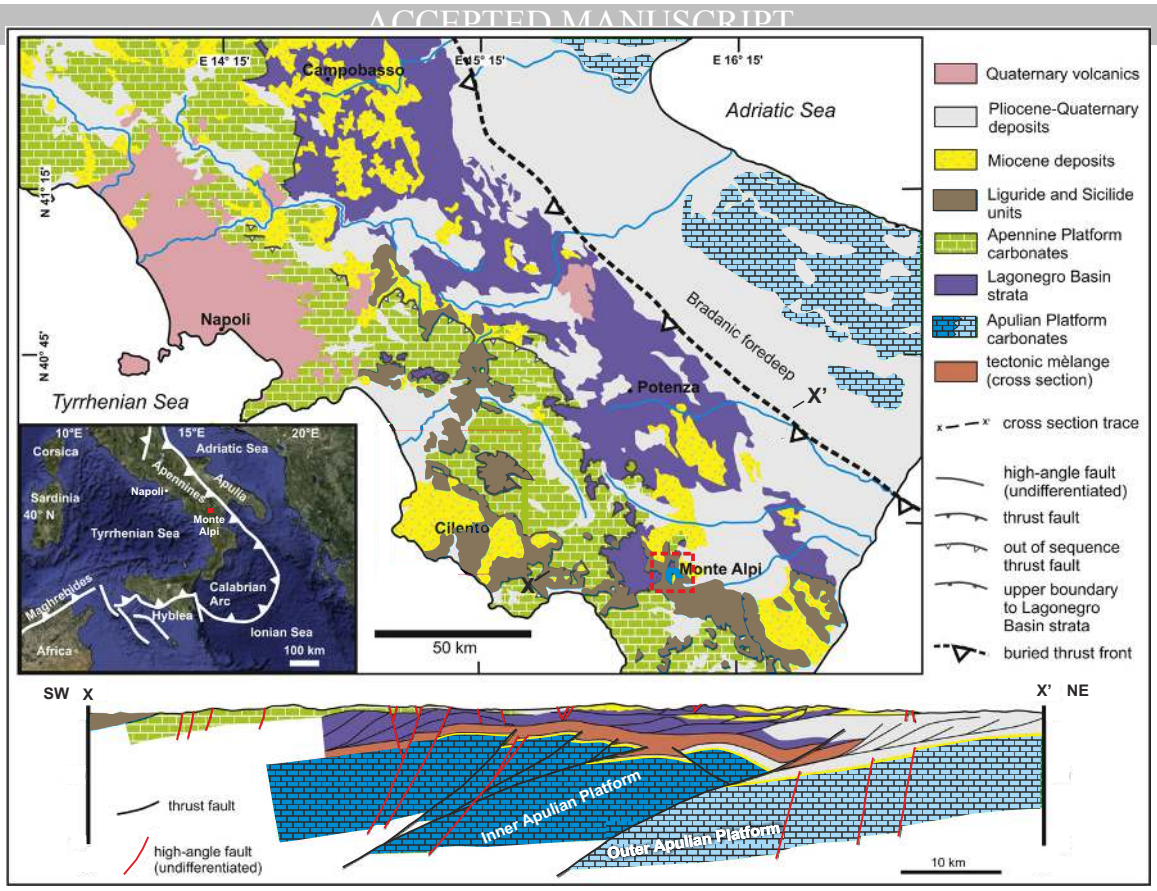

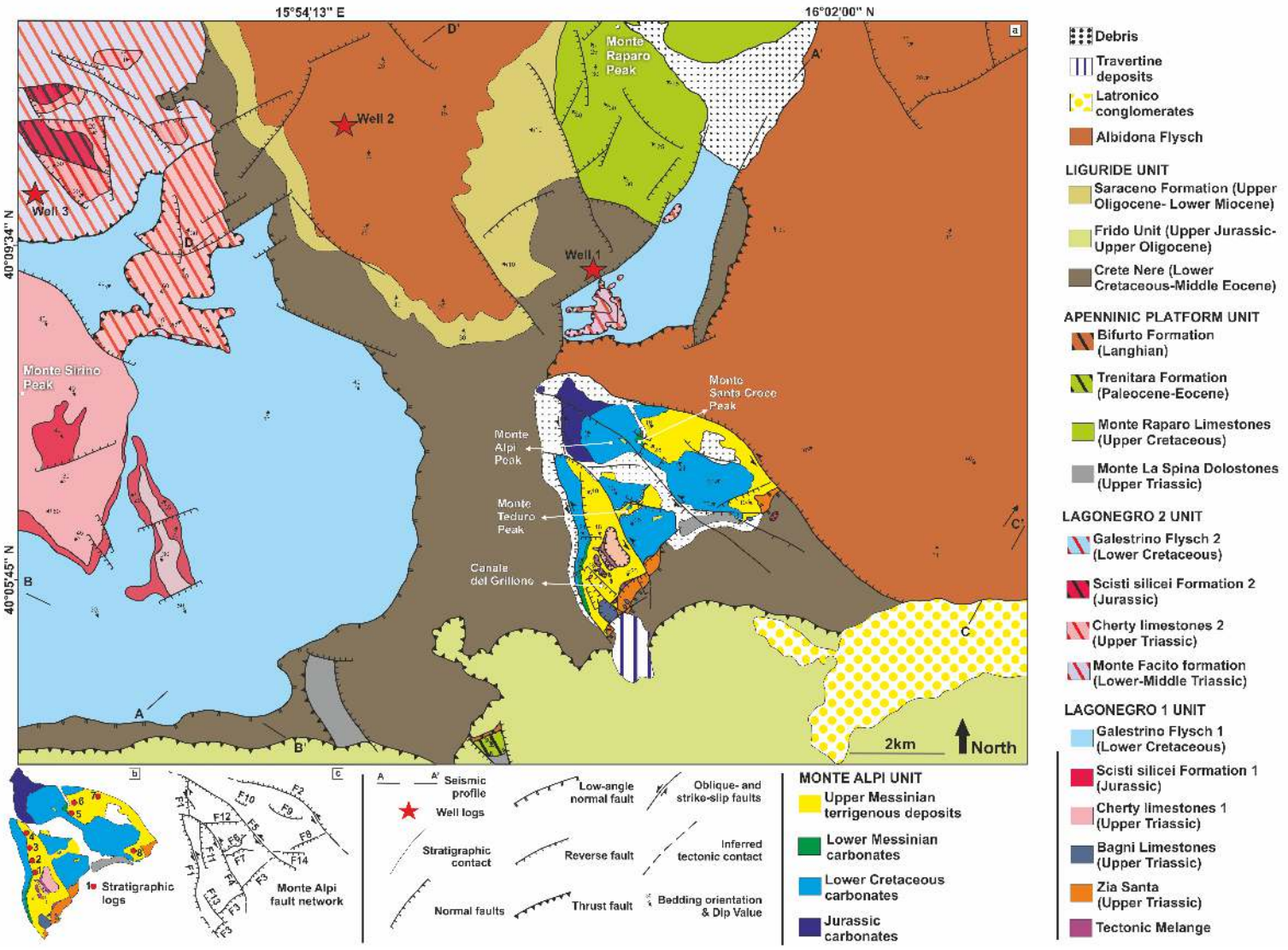
15°54'13" E
16°02'00" N
40°09'34" N
40°05'45" N
a
Well 1
Well 2
Well 3
Monte Raparo Peak
Monte Sirino Peak
Monte Santa Croce Peak
Monte Alpi Peak
Monte Teduro Peak
Canale del Grillone
A
A'
B
B'
C
C'
D
D'
2km
North
b
c
1 Stratigraphic logs
Monte Alpi fault network
Seismic profile
Well logs
Stratigraphic contact
Normal faults
Low-angle normal fault
Reverse fault
Thrust fault
Oblique- and strike-slip faults
Inferred tectonic contact
Bedding orientation & Dip Value
MONTE ALPI UNIT
Upper Messinian terrigenous deposits
Lower Messinian carbonates
Lower Cretaceous carbonates
Jurassic carbonates
Debris
Travertine deposits
Latronico conglomerates
Albidona Flysch
LIGURIDE UNIT
Saraceno Formation (Upper Oligocene- Lower Miocene)
Frido Unit (Upper Jurassic-Upper Oligocene)
Crete Nere (Lower Cretaceous-Middle Eocene)
APENNINIC PLATFORM UNIT
Bifurto Formation (Langhian)
Trenitara Formation (Paleocene-Eocene)
Monte Raparo Limestones (Upper Cretaceous)
Monte La Spina Dolostones (Upper Triassic)
LAGONEGRO 2 UNIT
Galestrino Flysch 2 (Lower Cretaceous)
Scisti silicei Formation 2 (Jurassic)
Cherty limestones 2 (Upper Triassic)
Monte Facito formation (Lower-Middle Triassic)
LAGONEGRO 1 UNIT
Galestrino Flysch 1 (Lower Cretaceous)
Scisti silicei Formation 1 (Jurassic)
Cherty limestones 1 (Upper Triassic)
Bagni Limestones (Upper Triassic)
Zia Santa (Upper Triassic)
Tectonic Melange

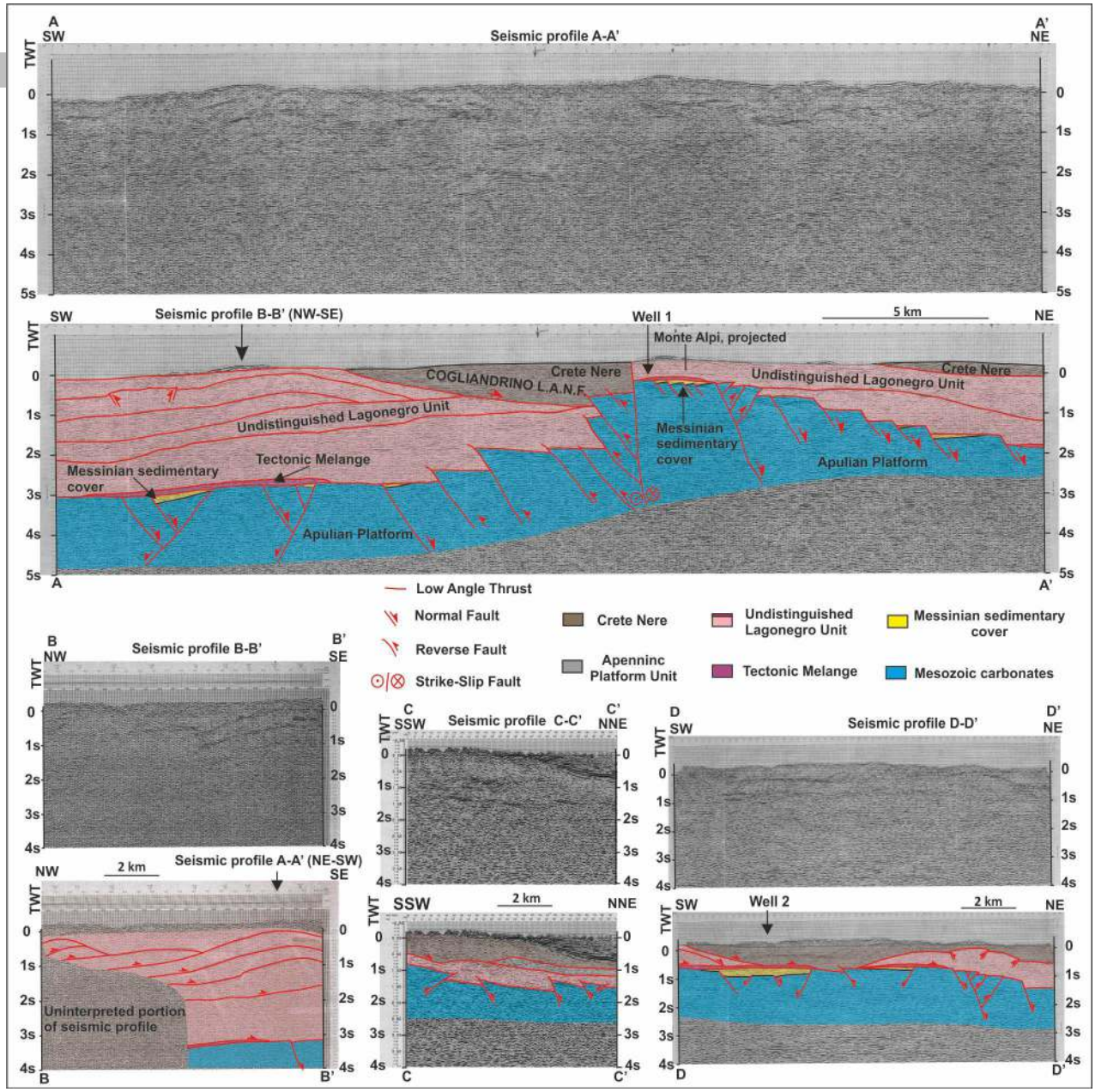
A
SW
Seismic profile A-A'
A'
NE
TWT
0
1s
2s
3s
4s
5s
SW
Seismic profile B-B' (NW-SE)
Well 1
5 km
NE
Monte Alpi, projected
COGLIANDRINO L.A.N.F.
Crete Nere
Undistinguished Lagonegro Unit
Messinian sedimentary cover
Tectonic Melange
Apulian Platform
A
A'
Low Angle Thrust
Normal Fault
Reverse Fault
Strike-Slip Fault
Crete Nere
Apenninc Platform Unit
Undistinguished Lagonegro Unit
Tectonic Melange
Messinian sedimentary cover
Mesozoic carbonates
B
NW
Seismic profile B-B'
B'
SE
2 km
Seismic profile A-A' (NE-SW)
Uninterpreted portion of seismic profile
C
SSW
Seismic profile C-C'
C'
NNE
D
SW
Seismic profile D-D'
D'
NE
Well 2

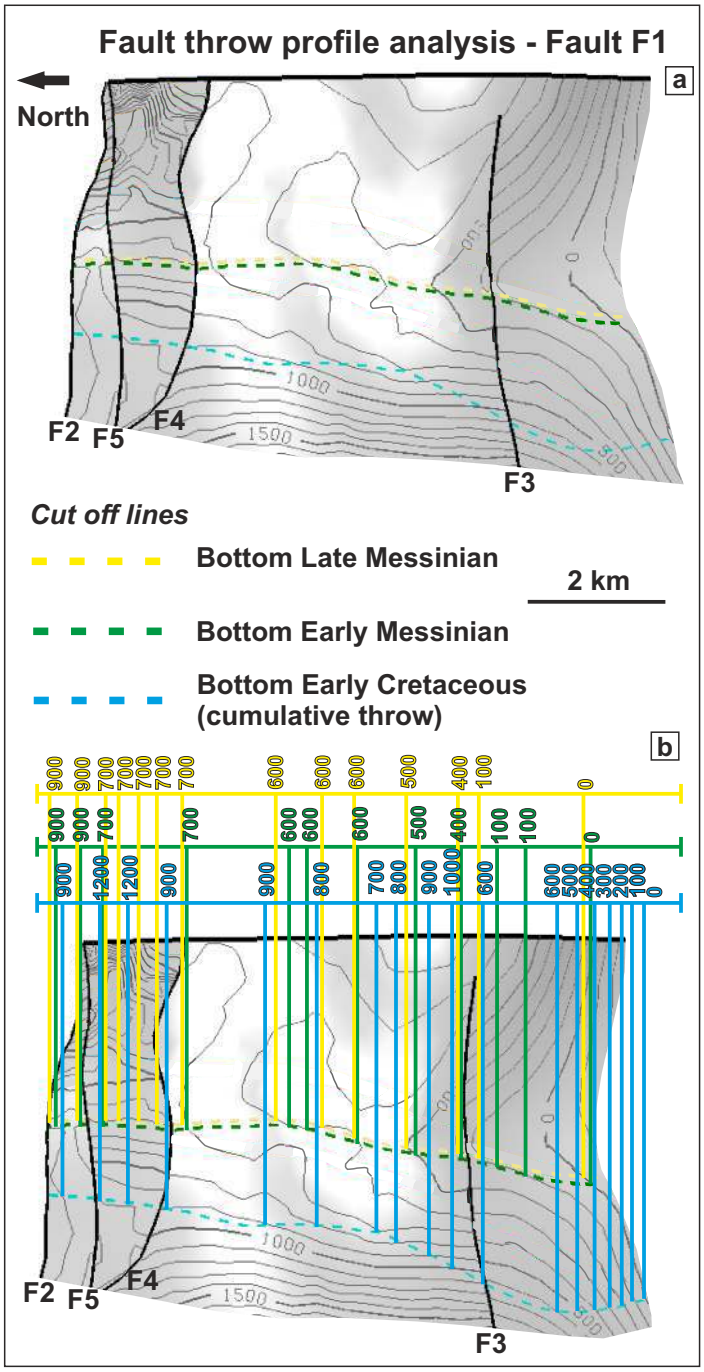
Fault throw profile analysis - Fault F1
North
a
F2
F5
F4
F3
1000
1500
Cut off lines
Bottom Late Messinian
2 km
Bottom Early Messinian
Bottom Early Cretaceous
(cumulative throw)
b
F2
F5
F4
F3
1000
1500

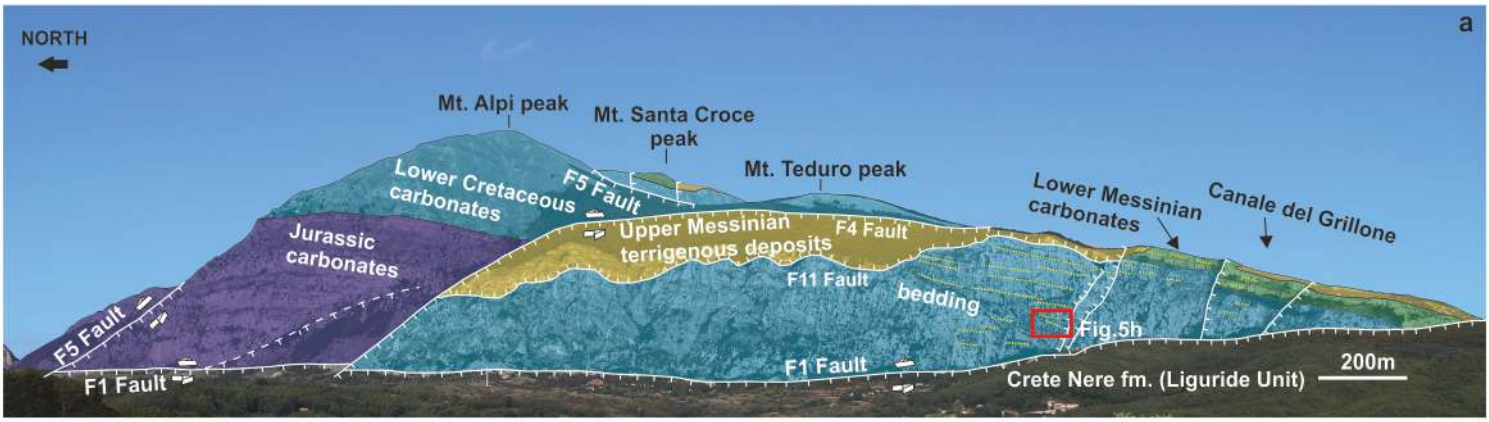

Legend

Jurassic carbonates | Lower Cretaceous carbonates | Lower Messinian carbonates | Upper Messinian terrigenous deposits

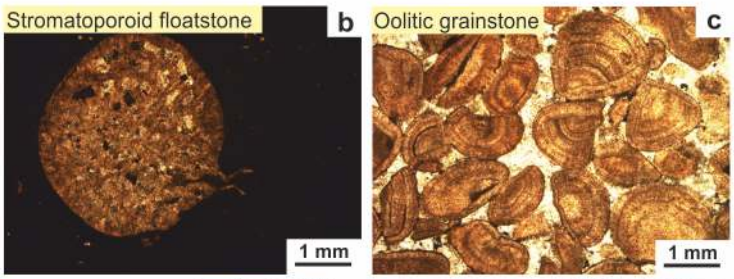

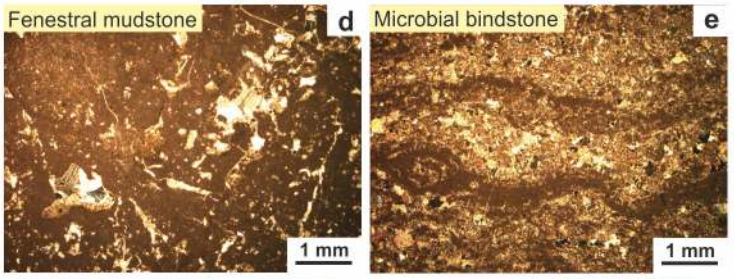

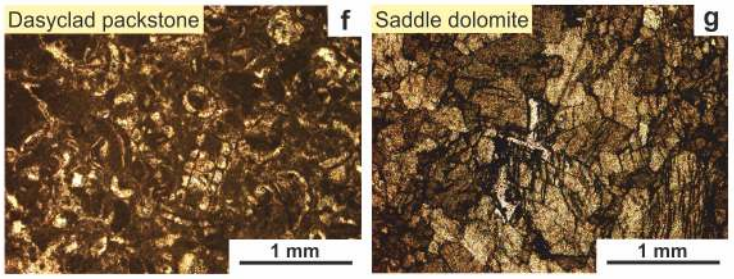

(b-f) = cross-polarized light; (g) = plane-polarized light

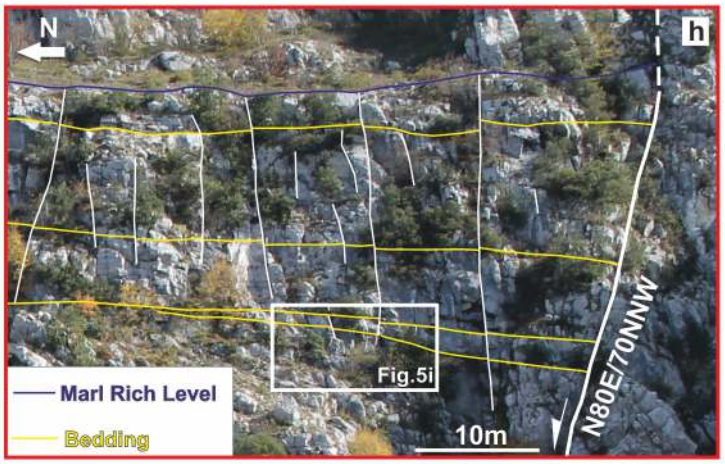

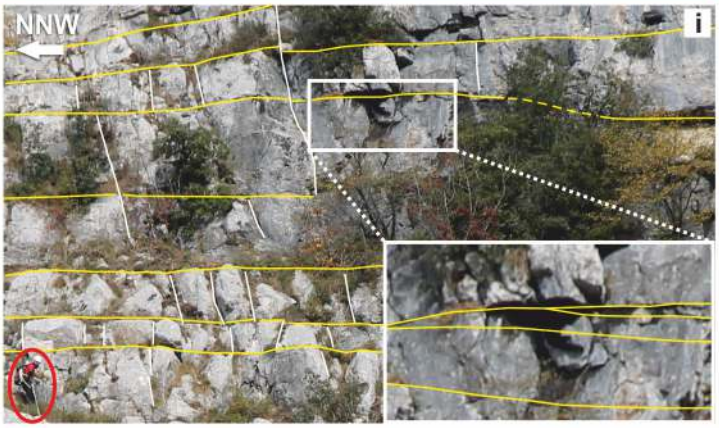

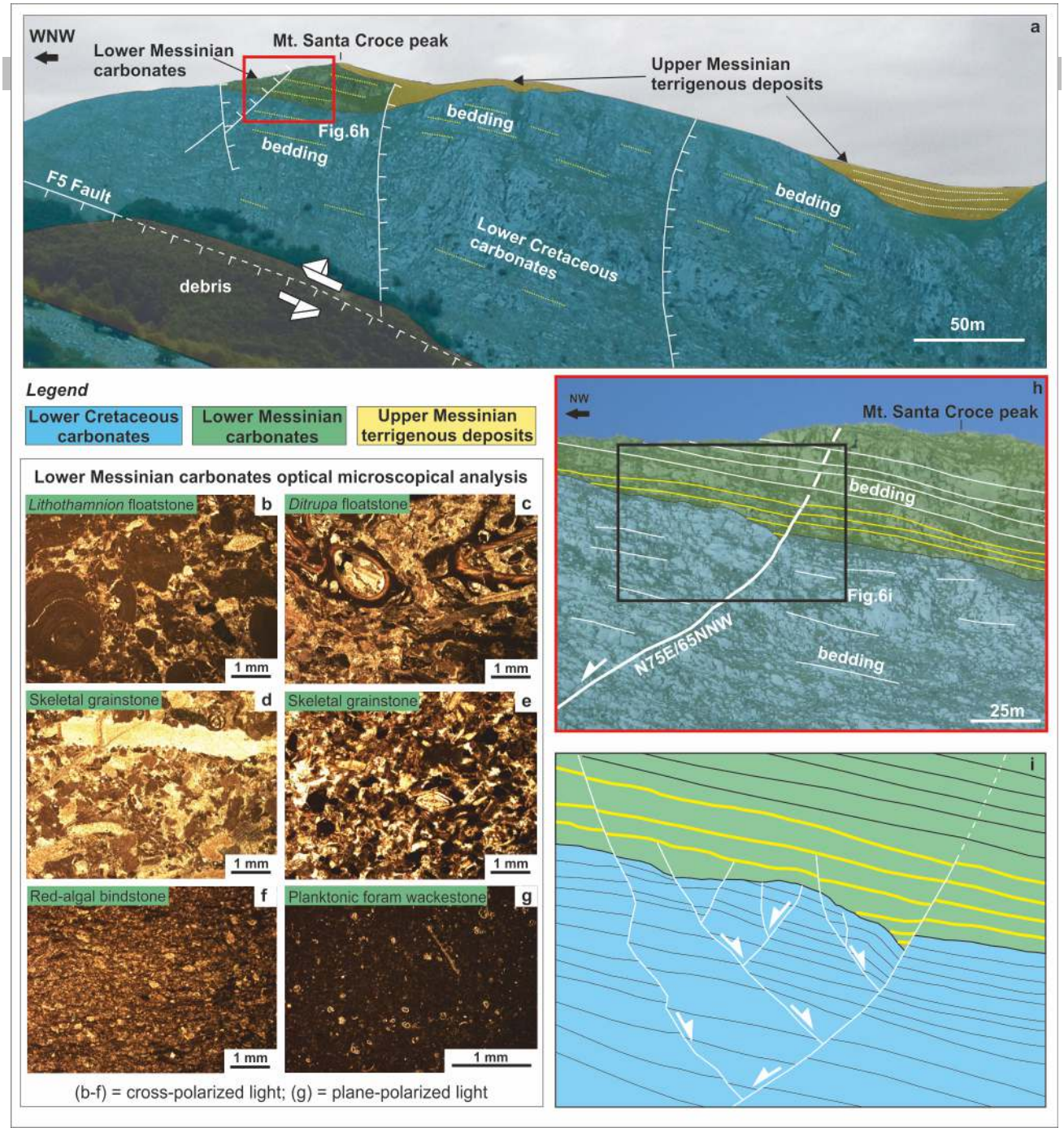
a
WNW
Lower Messinian carbonates
Mt. Santa Croce peak
Upper Messinian terrigenous deposits
Fig.6h
bedding
bedding
bedding
F5 Fault
Lower Cretaceous carbonates
debris
50m
Legend
Lower Cretaceous carbonates
Lower Messinian carbonates
Upper Messinian terrigenous deposits
Lower Messinian carbonates optical microscopical analysis
Lithothamnion floatstone
b
1 mm
Ditrupa floatstone
c
1 mm
Skeletal grainstone
d
1 mm
Skeletal grainstone
e
1 mm
Red-algal bindstone
f
1 mm
Planktonic foram wackestone
g
1 mm
(b-f) = cross-polarized light; (g) = plane-polarized light
h
NW
Mt. Santa Croce peak
bedding
Fig.6i
N75E/65NNW
bedding
25m
i


WEST
a
Monte Alpi Peak
Monte Teduro Peak
Fig. 7c
Lower Cretaceous carbonates
Upper Messinian conglomerates
bedding
bedding
10 m
Fault F11
NORTH
b
Monte Santa Croce Peak
Upper Messinian sandstones and conglomerates
bedding
bedding
Lower Messinian carbonates
Fig. 11e
50 m
Erosional surface
Fault F10
WEST
c
Conglomerates
NNW
d
bedding
Sandstones

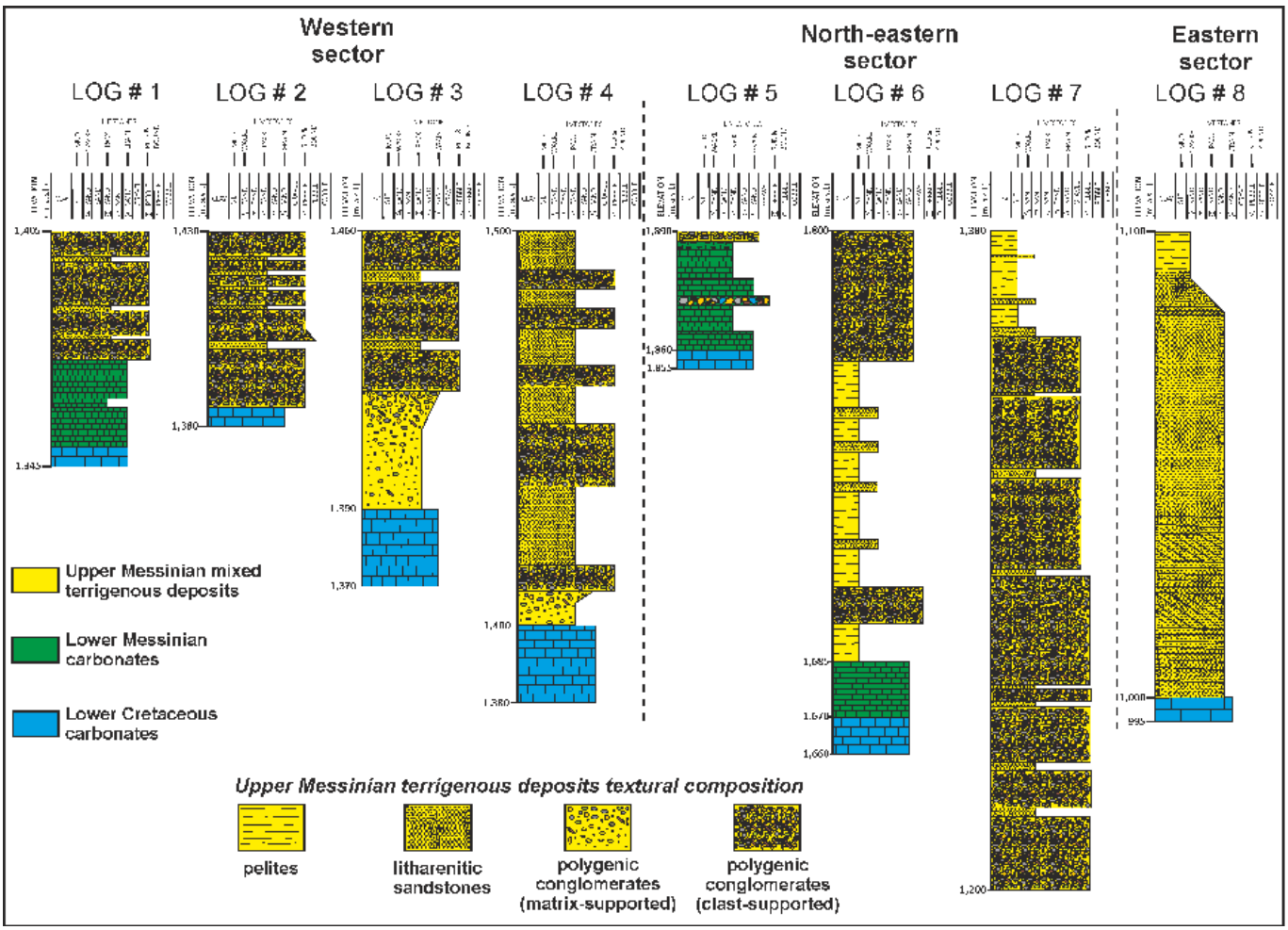
Western sector
North-eastern sector
Eastern sector
LOG # 1
LOG # 2
LOG # 3
LOG # 4
LOG # 5
LOG # 6
LOG # 7
LOG # 8
1,400
1,445
1,430
1,380
1,460
1,390
1,370
1,500
1,480
1,380
1,890
1,860
1,855
1,800
1,685
1,670
1,660
1,380
1,200
1,100
1,000
995
Upper Messinian mixed terrigenous deposits
Lower Messinian carbonates
Lower Cretaceous carbonates
Upper Messinian terrigenous deposits textural composition
pelites
litharenitic sandstones
polygenic conglomerates (matrix-supported)
polygenic conglomerates (clast-supported)

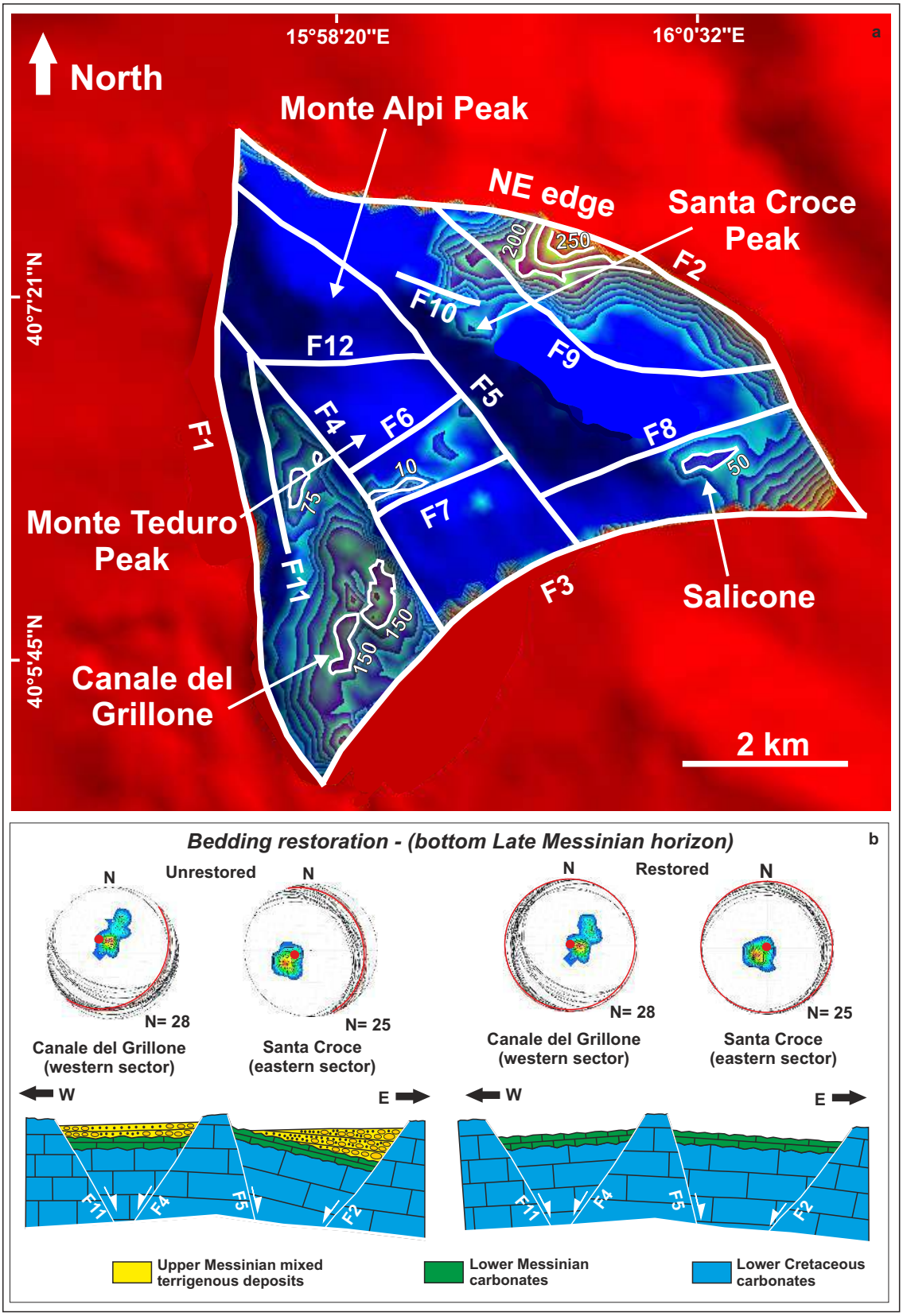
15°58'20"E
16°0'32"E
a
North
Monte Alpi Peak
NE edge
Santa Croce Peak
40°7'21"N
F2
F10
F12
F9
F5
F4
F6
F1
F8
10
75
50
F7
Monte Teduro Peak
F11
150
150
F3
Salicone
40°5'45"N
Canale del Grillone
2 km
b
Bedding restoration - (bottom Late Messinian horizon)
Unrestored
Restored
N
N= 28
N= 25
Canale del Grillone (western sector)
Santa Croce (eastern sector)
W
E
F11
F4
F5
F2
Upper Messinian mixed terrigenous deposits
Lower Messinian carbonates
Lower Cretaceous carbonates

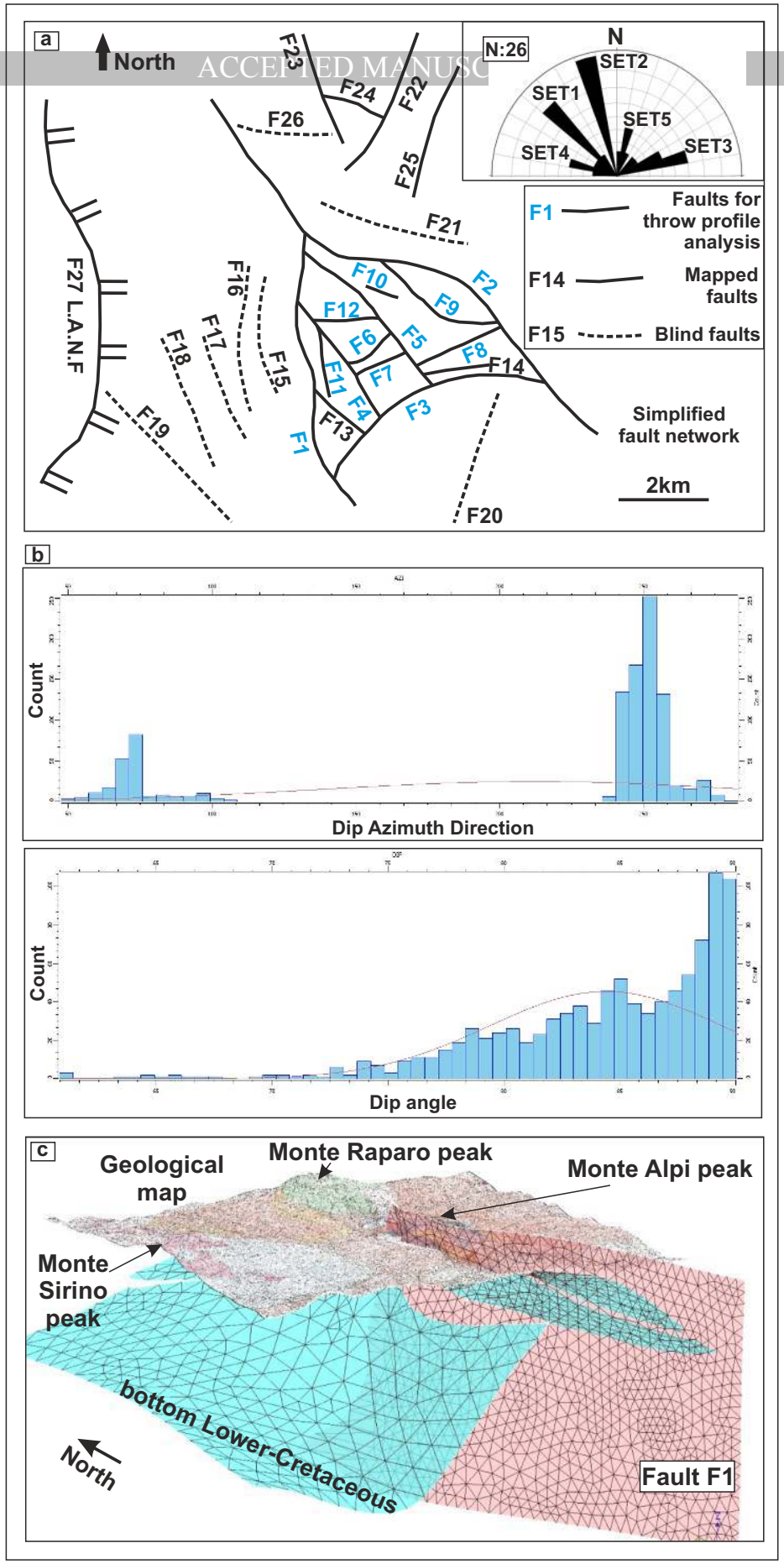

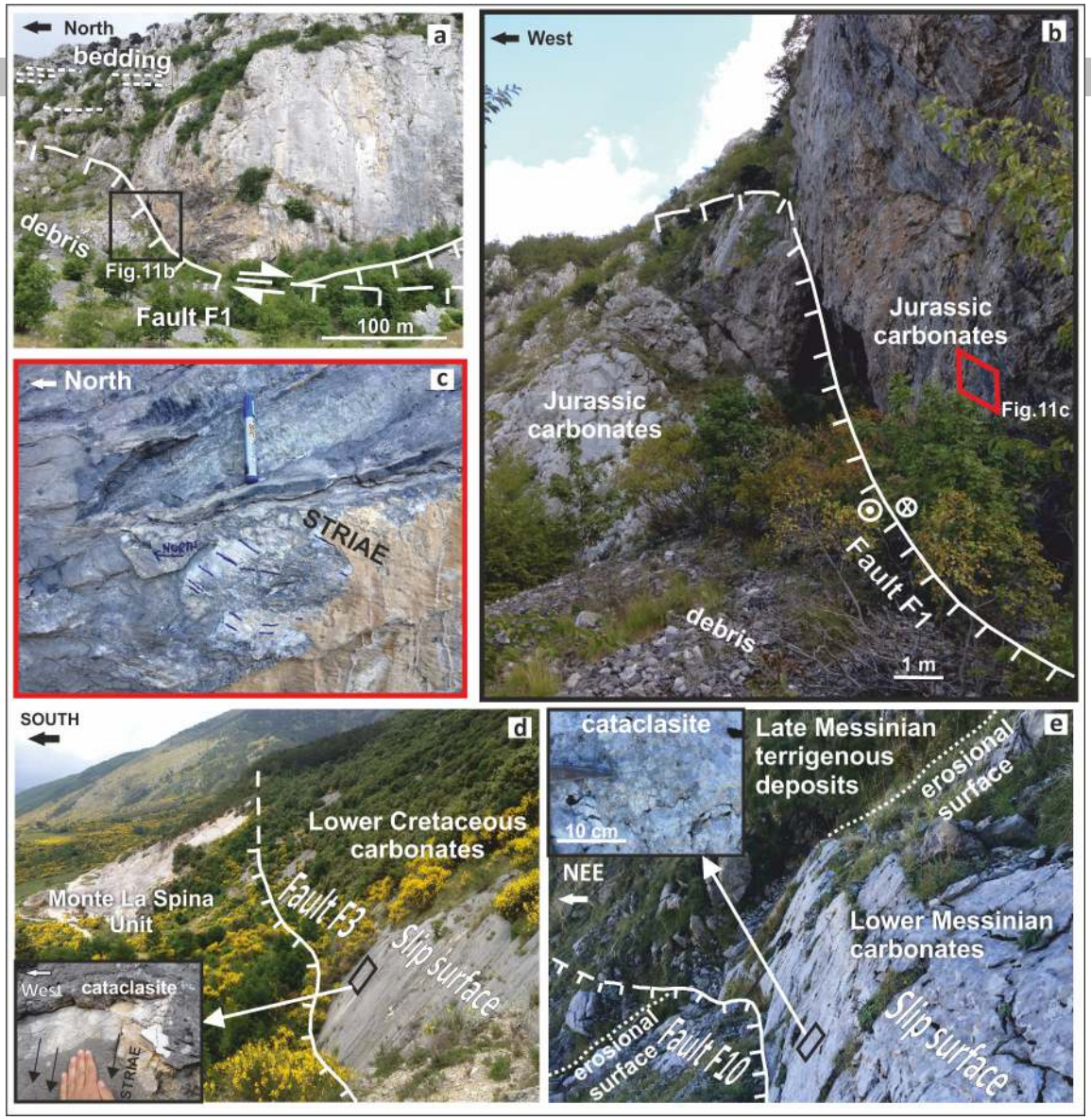
North
bedding
a
debris
Fig.11b
Fault F1
100 m
West
b
Jurassic carbonates
Jurassic carbonates
Fig.11c
Fault F1
debris
1 m
North
c
STRIAE
SOUTH
d
Lower Cretaceous carbonates
Monte La Spina Unit
Fault F3
Slip surface
West
cataclasite
STRIAE
cataclasite
10 cm
Late Messinian terrigenous deposits
erosional surface
e
NEE
Lower Messinian carbonates
erosional surface
Fault F10
Slip surface

CUMULATIVE THROW PROFILES

F1

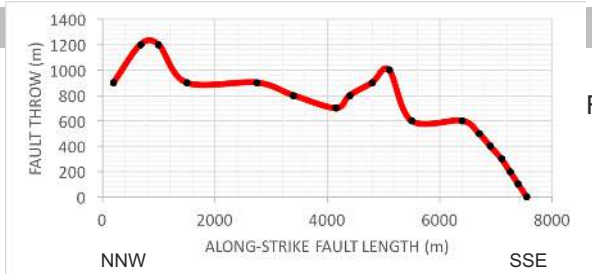

Fault Throw Error: ± 50m Fault Length Error: ± 50m

F7

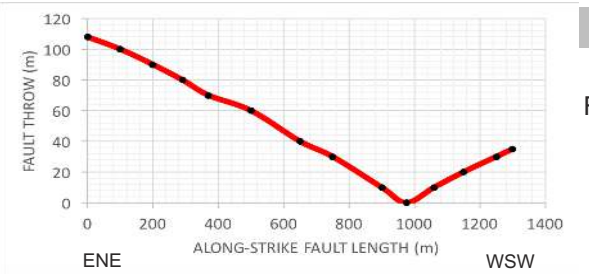

Fault Throw Error: ± 5m Fault Length Error: ± 25m

F2

Fault Throw Error: ± 50m Fault Length Error: ± 50m

F8

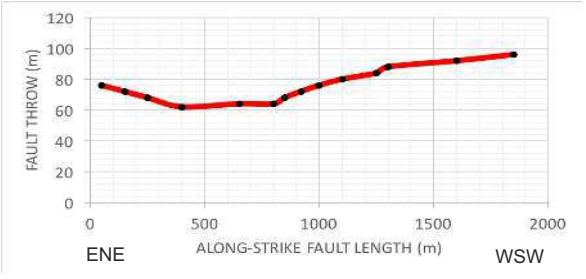

Fault Throw Error: ± 2m Fault Length Error: ± 25m

F3

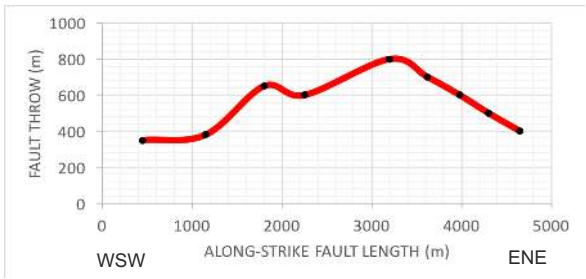

Fault Throw Error: ± 50m Fault Length Error: ± 50m

F9

Fault Throw Error: ± 5m Fault Length Error: ± 25m

F4

Fault Throw Error: ± 10m Fault Length Error: ± 25m

F10

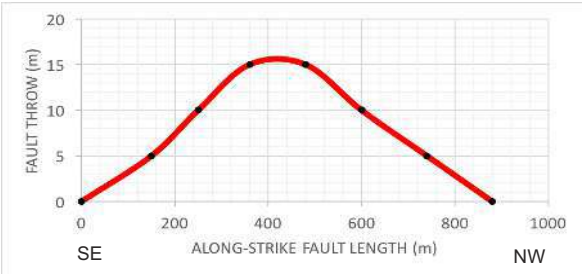

Fault Throw Error: ± 0.5m Fault Length Error: ± 25m

F5

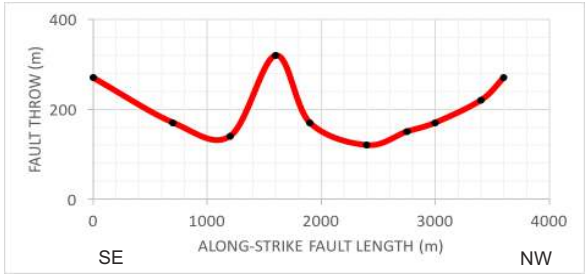

Fault Throw Error: ± 50m Fault Length Error: ± 50m

F11

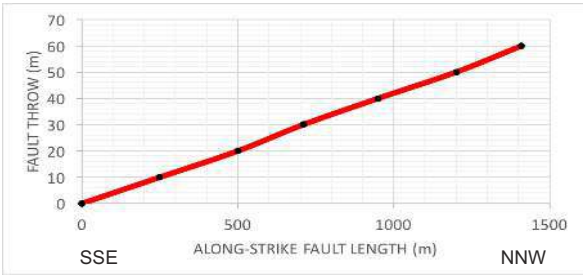

Fault Throw Error: ± 1m Fault Length Error: ± 50m

F6

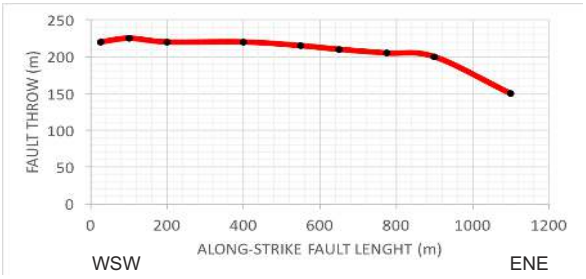

Fault Throw Error: ± 5m Fault Length Error: ± 25m

F12

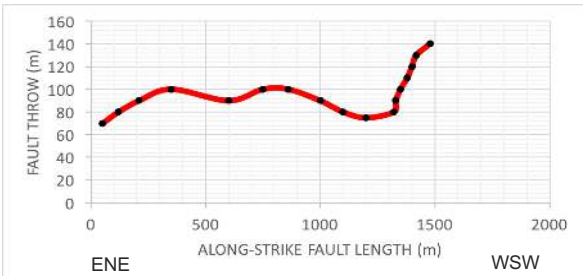

Fault Throw Error: ± 5m Fault Length Error: ± 50m

PRE-MESSINIAN, EARLY-MESSINIAN AND POST-EARLY MESSINIAN THROW PROFILES

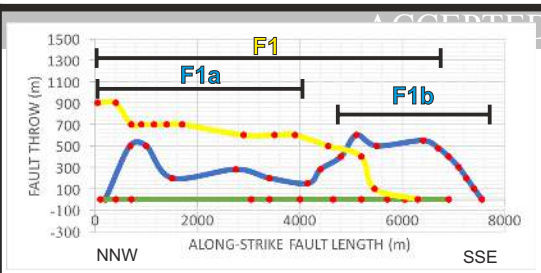

F1

Fault Throw Error: ± 50m Fault Length Error: ± 50m

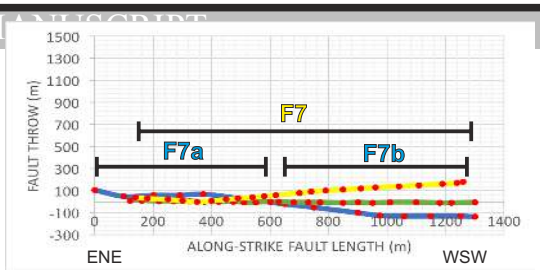

F7

Fault Throw Error: ± 5m Fault Length Error: ± 25m

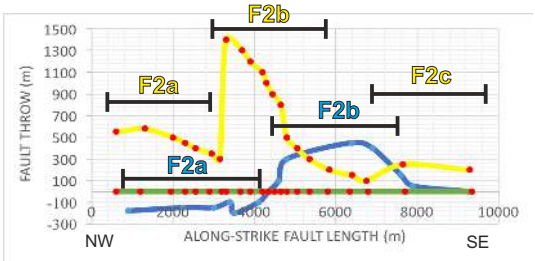

F2

Fault Throw Error: ± 50m Fault Length Error: ± 50m

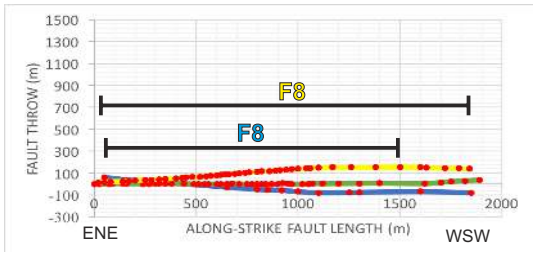

F8

Fault Throw Error: ± 2m Fault Length Error: ± 25m

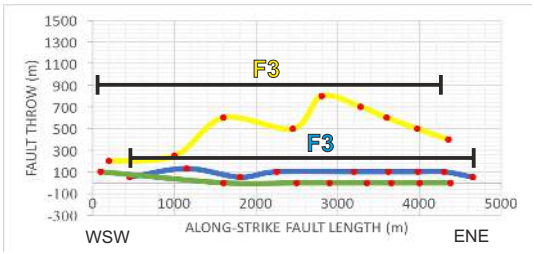

F3

Fault Throw Error: ± 50m Fault Length Error: ± 50m

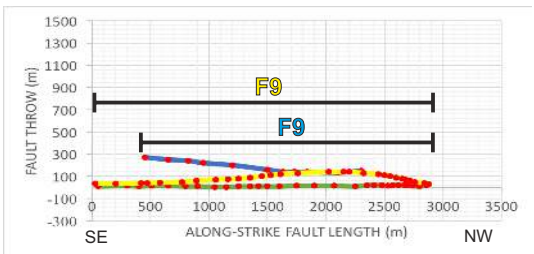

F9

Fault Throw Error: ± 5m Fault Length Error: ± 25m

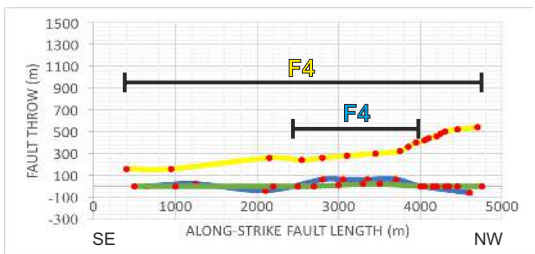

F4

Fault Throw Error: ± 10m Fault Length Error: ± 25m

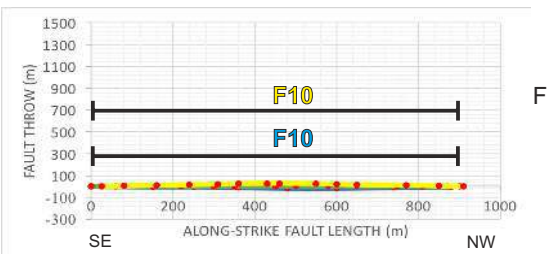

F10

Fault Throw Error: ± 0.5m Fault Length Error: ± 25m

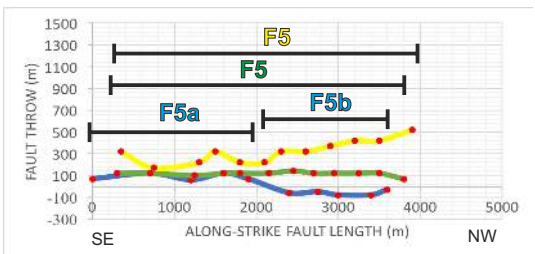

F5

Fault Throw Error: ± 50m Fault Length Error: ± 50m

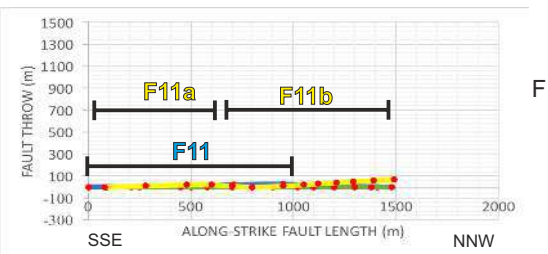

F11

Fault Throw Error: ± 1m Fault Length Error: ± 50m

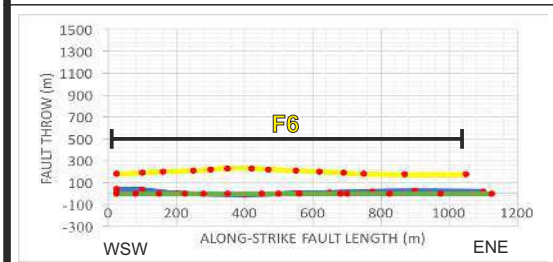

F6

Fault Throw Error: ± 5m Fault Length Error: ± 25m

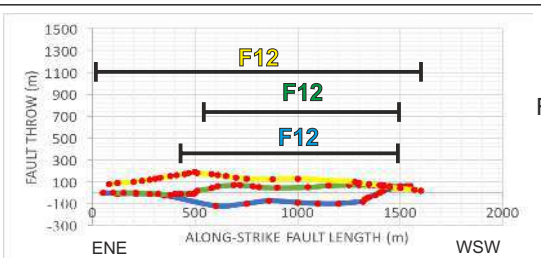

F12

Fault Throw Error: ± 5m Fault Length Error: ± 50m

Pre-Messinian	Early Messinian	Post-Early Messinian

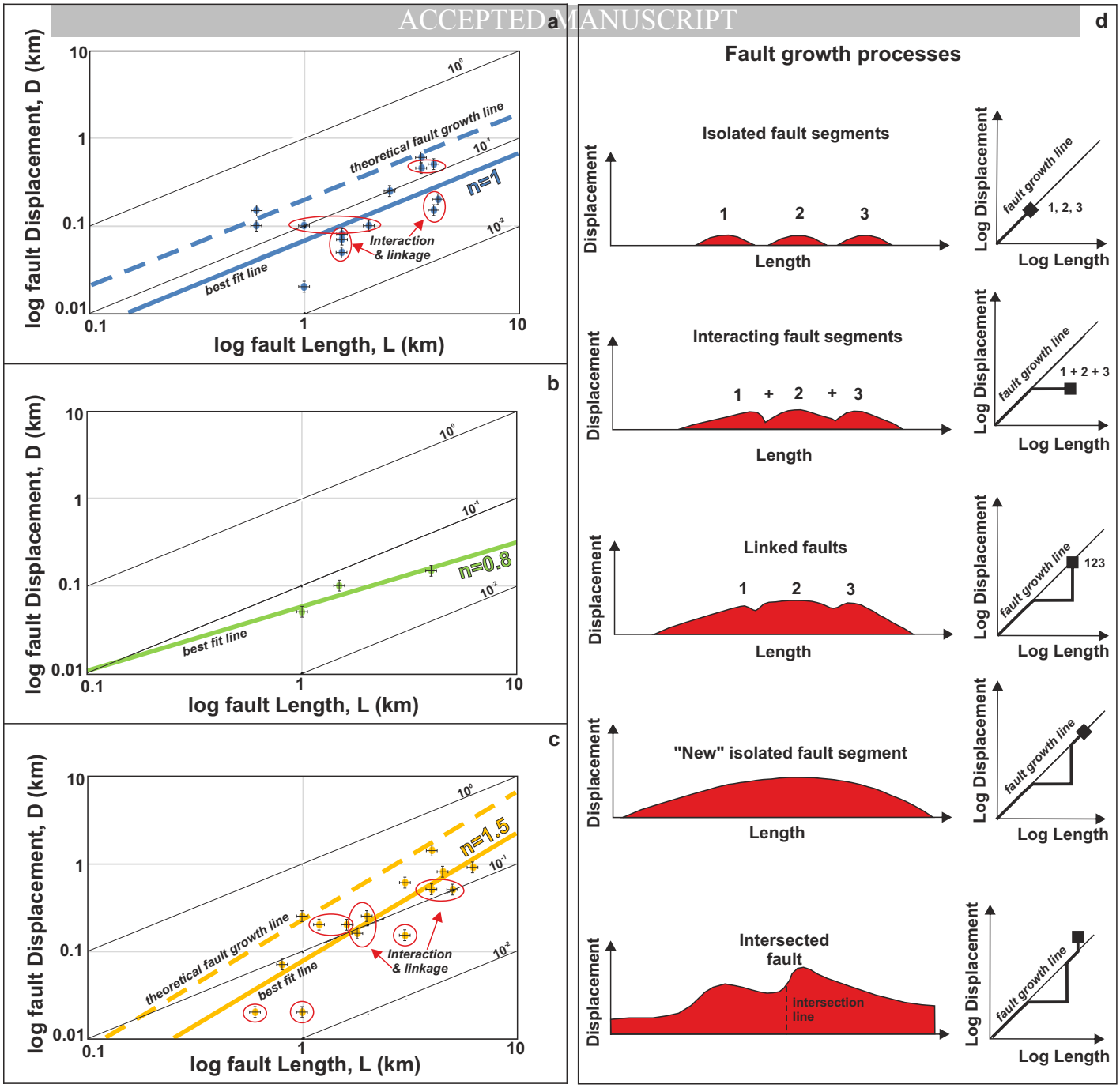

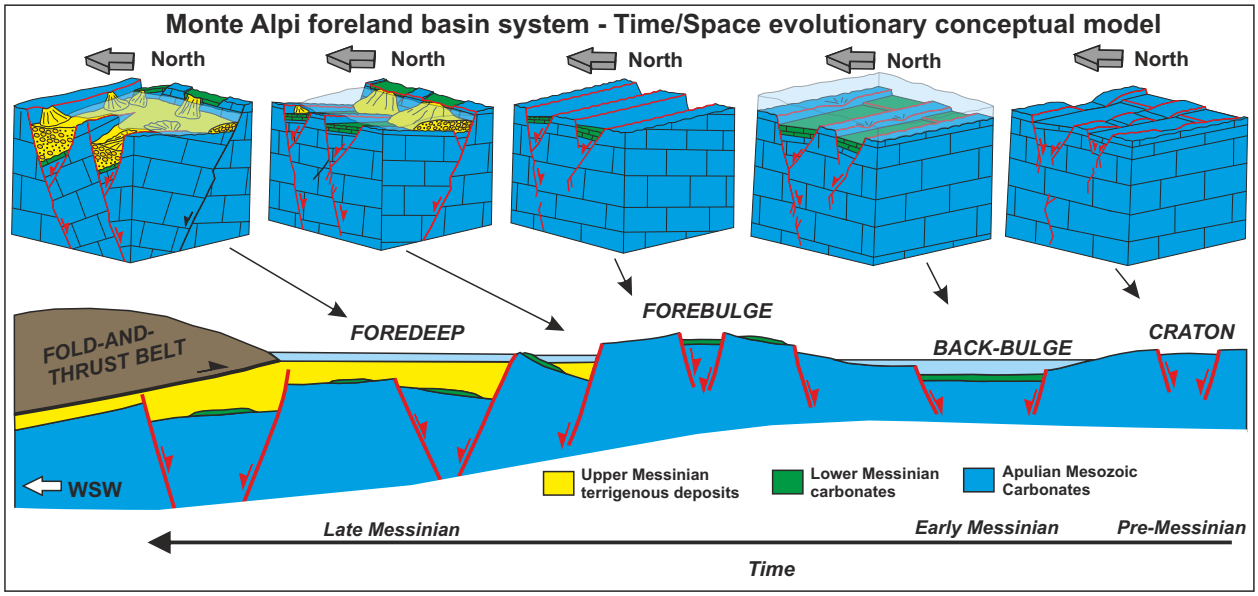
Monte Alpi foreland basin system - Time/Space evolutionary conceptual model
North
North
North
North
North
FOREDEEP
FOREBULGE
BACK-BULGE
CRATON
FOLD-AND-THRUST BELT
WSW
Upper Messinian terrigenous deposits
Lower Messinian carbonates
Apulian Mesozoic Carbonates
Late Messinian
Early Messinian
Pre-Messinian
Time

Highlights:

- Both timing and growth processes are deciphered for the pre-Pliocene fault network;
- Main dimensional attributes computed for all analyzed faults;
- Inferences on the fault-control evolution of the Messinian foreland basin system;